Alignable Lamella Gridshells

DAVIDE PELLIS, ISTI-CNR, Italy

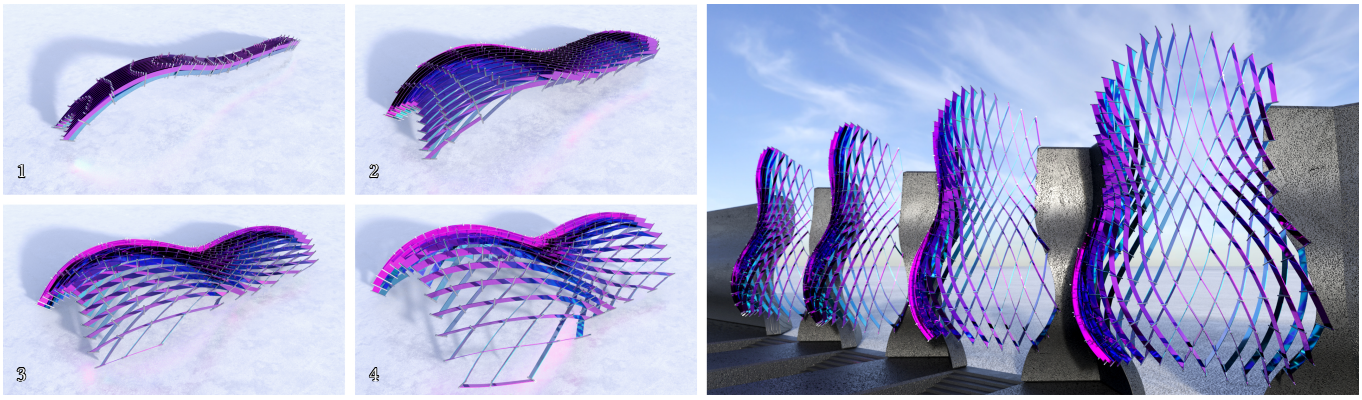

Fig. 1. This paper presents a computational pipeline for the inverse design of alignable lamella gridshells, which are deployable grid structures capable of collapsing into a planar curved strip. These structures can find applications in architecture, facilitating transportation and installation processes.

Alignable lamella gridshells are 3D grid structures capable of collapsing into a planar strip. This feature significantly simplifies on-site assembly and also ensures compactness for efficient transport and storage. However, designing these structures still remains a challenge. This paper tackles the inverse design problem of alignable lamella gridshells leveraging concepts from differential geometry and Cartan's theory of moving frames. The study unveils that geodesic alignable gridshells, where lamellae are disposed tangentially to the surface, are limited to forming shapes isometric to surfaces of revolution. Furthermore, it demonstrates that alignable gridshells with lamellae arranged orthogonally to a surface can be realized only on a specific class of surfaces that meet a particular curvature condition along their principal curvature lines. Finally, drawing on these theoretical findings, this work introduces novel computational tools tailored for the design of these structures.

CCS Concepts: • **Computing methodologies** → **Shape modeling**.

Additional Key Words and Phrases: Architectural Geometry, Deployable Structures, Gridshells, Computational Fabrication, Inverse Design

ACM Reference Format:
Davide Pellis. 2024. Alignable Lamella Gridshells. *ACM Trans. Graph.* 43, 6, Article 183 (December 2024), 20 pages. https://doi.org/10.1145/3687898

1 INTRODUCTION

Gridshells are architectural structures that combine the mechanical efficiency of a continuous shell with the construction simplicity of a grid-like structure. Conventional gridshells are assembled by connecting rigid beam elements at joints to form a given shape. However, this construction process typically involves temporary supports, impacting overall cost. An alternative solution are *deployable elastic gridshells*, which can be assembled in a planar state and brought into shape through elastic deformation of beams and rotations at connection joints. This deployment is typically achieved through lifting or other point-wise actuation methods. Moreover, if the planar state is sufficiently compact, the structure can be assembled off-site and transported with ease.

The final shape assumed by a deployable elastic gridshell is determined by its planar layout and also by the mechanical properties of its beams. This complex interplay makes designing these structures a challenging task. A possible design strategy involves the integration of physical simulation techniques with optimization algorithms, as shown in the work of Panetta et al. [2019]. The main advantage of this methodology lies in its ability to capture the actual behavior of the structure. However, simulation-based approaches have some drawbacks, including high computational costs and limitations in handling inverse design tasks (i.e., finding a beam layout given a deployed shape).

When beams have a marked flat profile, assuming the form of 'lamellae', it becomes possible to determine the deployed shape through purely geometric considerations. Indeed, for such beams we can make the assumptions of inextensibility and resistance to bending only along the wider cross-sectional direction. For instance, under these assumptions, a straight lamella bent with its width arranged orthogonally to a surface follows an asymptotic curve. Conversely, when the same lamella is disposed tangentially to a surface, its axis traces a geodesic curve. More generally, the axes of lamellae disposed on a surface with a consistent orientation yield a network of curves with specific geometric properties. In the following, we refer to these structures as *lamella gridshells*. Although a geometric approach to designing lamella gridshells may have limitations in terms of physical accuracy, it involves simpler computations and facilitates inverse design. Additionally, it can serve as an initial step for simulation-based methodologies like [Panetta et al. 2019].

Author's address: Davide Pellis, davide.pellis@isti.cnr.it, ISTI-CNR, Italy.

A notable category of *deployable* lamella gridshells, which can be designed with a purely geometric approach, relates to *alignable nets*. Recently introduced by Tellier [2022a,b], alignable nets are quadrilateral networks of curves interconnected at joints, capable of collapsing into a line while preserving their lengths. By imposing constraints on the normal or geodesic curvatures of an alignable net, it becomes possible to capture the behavior of deployable lamella gridshells. For instance, geodesic and asymptotic alignable nets can serve as axes of lamella gridshells that collapse into a straight segment, while enforcing a constant normal curvature results in lamella gridshells that collapse into a circular arc.

However, while alignable nets can locally cover arbitrary surfaces, imposing constraints on the normal and geodesic curvatures introduces limitations on the range of shapes effectively covered by these nets. Understanding these shape constraints is crucial for enabling the inverse design of alignable lamella gridshells: Indeed, this approach allows us to split the design process into a first surface optimization step followed by curves tracing, overcoming challenges associated with an unknown beam layout.

A special subset of alignable nets are the so-called Chebyshev nets, characterized by equal curve lengths between joints. In their recent work, Liu et al. [2023] outlined the classes of surfaces on which Chebyshev nets with constrained normal curvature exist. These nets permit the extraction of lamella gridshells disposed orthogonally to the surface and capable of collapsing into a planar curve. However, the corresponding classes of surfaces on which generic alignable nets exist still remain undefined.

To address this gap, this work focuses on the inverse design of generic alignable lamella gridshells. First, it outlines the classes of surfaces which can be covered by geodesic alignable nets and alignable nets with constrained normal curvature, thus allowing the extraction of lamella gridshells capable of collapsing into planar curves. Then, exploiting these insights, this work introduces computational pipelines tailored to the design of such alignable lamella gridshells.

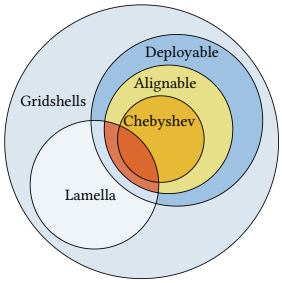

Fig. 2. Classification of gridshells adopted in this paper. Alignable lamella gridshells are highlighted in *red*.

1.1 Related work

1.1.1 Deployable structures. This research is situated within the domain of optimization-based design for deployable shell structures. In this context, various systems have been proposed for deploying shell structures from planar or compact configurations. Examples include pre-tensioned membranes [Guseinov et al. 2017; Pérez et al. 2017], scissor mechanisms [Ren et al. 2022; Van Mele et al. 2010], inflatable tube structures [Panetta et al. 2021], auxetic materials [Chen et al. 2021; Konaković et al. 2016], bending active patterns [Laccone et al. 2021], and 2D strip patterns [Hong et al. 2022; Mhatre et al. 2021].

Closely related to deployable elastic gridshells is the work by Panetta et al. [2019]. They propose a computational method that takes as input a planar grid of straight beams with specified cross-sections. Their pipeline begins with simulating the deployment of the grid, considering the elastic energy stored in the beams. Subsequently, the planar grid is optimized for target functions such as minimal elastic energy and fitting to a predefined shape by computing derivatives with respect to the planar configuration. This methodology has been extended to address deployable gridshells with curved beams in [Becker et al. 2023]. This last work introduces an additional inverse design procedure that relies on preserving lengths within a predetermined connectivity.

1.1.2 Lamella gridshells. Lamella gridshells are structures composed of developable or nearly-developable strips arranged in a grid forming a 3D surface. The computational design of these structures draws upon tools from differential geometry of curve networks on surfaces and their discrete equivalents, systematically explored in [Bobenko and Suris 2008].

Geodesic gridshells, characterized by lamellae tangent to the surface, have received considerable attention in computational design for efficient fabrication [Kahlert et al. 2011; Pottmann et al. 2010]. In this context, Wang et al. [2019] introduced a mesh-based methodology for generating smooth networks of geodesic curves on surfaces, well-suited for architectural applications. Asymptotic gridshells, where lamellae are arranged orthogonally to the surface, have been investigated by Schling et al. [2018]. Subsequently, Schling et al. [2022] explored hybrid geodesic-asymptotic gridshells, combining lamellae oriented orthogonally and tangentially to the surface. Pseudo-geodesic gridshells, composed of straight lamellae arranged at a given inclination with respect to the surface, have been addressed in [Wang et al. 2023].

Besides straight lamellae, Ren et al. [2021] explored gridshells constructed by weaving curved lamellae tangentially to the surface, while Pellis et al. [2020] investigated gridshells made of circular lamellae arranged orthogonally to the surface, using a mesh discretization approach. Furthermore, Hafner and Bickel [2021] investigated the use of lamellae with varying width, following elastic curves.

1.1.3 Chebyshev nets. The simplest category of geometrically deployable elastic gridshells is based on regular grids, which are curve networks where the lengths between adjacent joints are equal. These structures, called *Chebyshev nets*, derive their name from the mathematician Pafnutij Chebyshev, who investigated surface covering techniques using fabrics [Chebyshev 1878]. From a geometric standpoint, a Chebyshev net is an assembly of surface patches that are parameterized by two unit-speed parameters. Locally, a Chebyshev net exists around each point of a surface, and patchworks of Chebyshev nets can approximate arbitrary shapes [Garg et al. 2014; Sageman-Furnas et al. 2019]. The work by Masson and Monasse [2017] has recently demonstrated that it is always possible to cover a surface with a single patch of a Chebyshev net, provided the integral of its Gaussian curvature is less than 2π. The orientation of a single

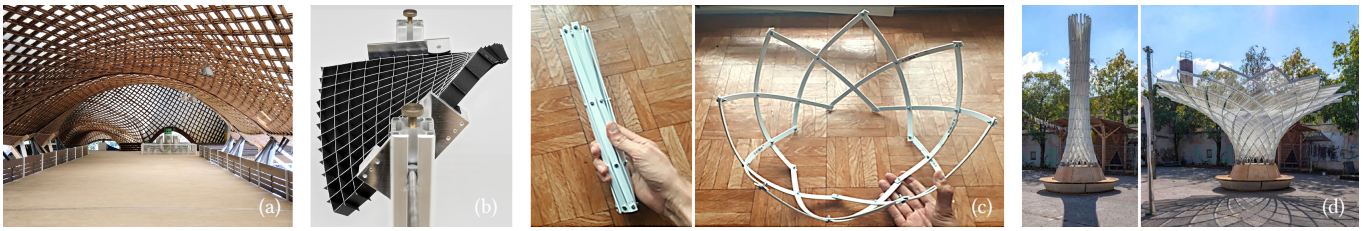

Fig. 3. (a) 'Mannheim Multihalle': The structure shapes a Chebyshev net. The deployment alters the curvature of the beams and the angles of the net. The final shape is achieved by securing the boundary in a predetermined position (CC BY 3.0 H. Berberich). (b) A lamella gridshell based on an asymptotic Chebyshev net, from [Liu et al. 2023]. Such a net exists only on surfaces with constant negative Gaussian curvature (K-surfaces). (c) A geodesic alignable net with rotational symmetry, from [Tellier 2022a]. (d) 'Kinetic Umbrella' by Jonas Schikore and Eike Schling. This mechanism leverages an asymptotic alignable net with rotational symmetry (© J. Schikore).

patch on a given surface is constrained by the underlying hyperbolic equations, allowing for the specification of its orientation along only two of its boundaries.

A pioneering example of an elastic deployable gridshell based on a Chebyshev net is the Mannheim 'Multihalle', designed by Otto Frei and built in 1975 (see Figure 3a). Recent applications include the gridshell for the Solidays festival in Paris [Naicu et al. 2014] and the the 'Ephemeral Cathedral' of Créteil [Du Peloux et al. 2015]. In this kind of gridshells, during deployment beams maintain their lengths while experiencing changes in their geodesic and normal curvatures.

By constraining the geodesic or normal curvatures of a Chebyshev net, we can model deployable lamella gridshells. It is well-known that a geodesic Chebyshev net can only shape developable surfaces, while asymptotic Chebyshev nets exist only on surfaces with constant negative Gaussian curvature, called K-surfaces (see Figure 3b). Chebyshev nets with constant normal curvature have been the focus of recent investigation [Liu et al. 2023]. In this study, the authors establish that such nets exist exclusively on linear Weingarten surfaces of hyperbolic type, which are offsets of K-surfaces. These nets, if materialized with lamellae disposed orthogonally to the surface, can be collapsed into a planar circular strip. This work also demonstrates that normal curvature-preserving Chebyshev nets, which collapse into a generic planar curve, are surprisingly more constrained as they can only shape rotational and cylindrical surfaces.

1.1.4 Alignable nets. By relaxing the constraint of equal lengths between joints, we encounter a broader category of deployable curve networks known as *alignable nets*. These nets are defined by the property that any quadrilateral loop of curves between joints can be collapsed into a single line, without altering the lengths of the curves. Alignable nets have been introduced in recent works by Tellier [2022a,b]. In these studies, the alignability of a net is characterized through the coefficients of the first fundamental form of a surface parametrization and their derivatives. These works also present simple examples of geodesic alignable nets built on surfaces of revolution (see Figure 3c). Similarly, Jonas Schikore and Eike Schling employed an asymptotic alignable net with rotational symmetry for their 'Kinetic Umbrella' [Schling and Schikore 2023] (see Figure 3d).

Soriano et al. [2019] addressed the design of geodesic gridshells that can be deployed from a flat state while maintaining constant lengths between joints. In most of the examples presented in their paper, the planar configuration closely resemble a straight line, suggesting that the resulting net could be considered approximately alignable. Their method involves approximating a target surface using an elastic gridshell with predetermined connectivity, leveraging length preservation.

Another noteworthy approach for designing 'closely-alignable' geodesic gridshells has been introduced by Pillwein et al. [2020]. While this method effectively approximates a given target shape and its boundaries, it does not preserve lengths between joints during the deployment, necessitating the introduction of sliding connections.

1.2 Overview and contribution

This work investigates the design of alignable lamella gridshells by exploring the geometric properties of alignable nets and the surfaces they define.

Section 2 provides a concise overview of curves on surfaces and their analysis using Cartan's method of moving frames. Then, it introduces a novel approach for investigating non-orthogonal curve nets based on a double moving frame.

Section 3 delves into the differential geometry of alignable nets through the application of the double moving frame framework. After establishing the necessary conditions for a curve net to be alignable, this section systematically investigates the conditions under which a surface permits the existence of geodesic alignable nets and normal curvature-preserving alignable nets (see Figure 4). The latter include constant normal curvature and asymptotic nets. To the best of the author's knowledge, these conditions are presented here for the first time. A summary of the contributions of this section, compared to the known equivalent conditions for Chebyshev nets, is provided in Table 1.

In Section 4, two computational methods for designing alignable lamella gridshells are presented, each tailored to a specific class of lamellae. The first method, designed for geodesic lamellae, utilizes a state-of-the-art technique [Wang et al. 2019], while the second method, developed for normal curvature-preserving lamellae, incorporates a novel implementation based on a previous approach developed for Weingarten surfaces [Pellis et al. 2021]. This section also introduces a method for curves tracing based on level-sets of a B-spline function, a post-optimization procedure based on a mesh

Table 1. Conditions for the existence of alignable nets in relation to the net surface. Conditions established in prior works are represented in *black*, while the conditions demonstrated in this study are highlighted in *yellow*. None = no constraints of curvatures. GG = geodesic net, AA = asymptotic net, CNC = constant normal curvature net, NCP = normal curvature-preserving net.

	Chebyshev	**Alignable**
None	All surfaces	All surfaces
GG	Developable	Theorem 1
AA	K-surfaces	Corollary 3
CNC	Hyperbolic linear Weingerten	Corollary 2
NCP	Cylindrical and rotational	Theorem 2

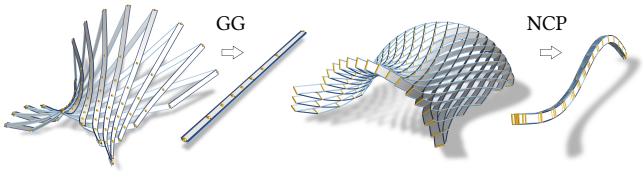

Fig. 4. On the *left*: A geodesic (GG) alignable gridshell collapses into a straight strip. On the *right*: A normal curvature-preserving (NCP) alignable gridshell collapses into a strip shaping a planar curve. This latter type encompasses both constant normal curvature (CNC) and asymptotic (AA) alignable gridshells, collapsing respectively in a circular and a straight strip.

discretization, and a deployment simulation which leverages geometric constraints. Finally, in Section 5, the achieved results are presented and discussed.

2 CURVE NETS

To study alignable nets, we leverage Cartan's theory of moving frames. At the core of this methodology lies the use of differential forms to study the evolution of a unit tangent frame along a curve net on a surface. A notable advantage of this formulation is that all derived quantities come with well-defined geometric interpretations, offering valuable insights for our investigation. For readers who may be unfamiliar with differential forms, a concise introduction is provided in Appendix A — recommended before proceeding to this section. For a more in-depth understanding of Cartan's theory of surfaces, readers can consult textbooks such as [O'Neill 2006] and [Needham 2021].

2.1 Notation

This study focuses on smooth curves, denoted by C, and smooth surfaces, denoted by $\mathcal{S}$, embedded in Euclidean space. Points in space are represented by uppercase Roman letters, such as P and Q. Scalar values, including angles, are denoted by lowercase letters — both Greek and Roman[1]. Vectors are represented by lowercase bold Roman letters, such as $\mathbf{v}$ and $\mathbf{w}$, while forms are indicated by lowercase bold Greek letters, like $\boldsymbol{\omega}$ and $\boldsymbol{\nu}$.

[1]In adherence to notation conventions, exceptions include the Gaussian and mean curvature of a surface, as well as the coefficients of parametrization fundamental forms, indicated using uppercase Roman letters.

At any point $P \in \mathcal{S}$, the tangent plane of the surface is denoted as $T_{\mathcal{S}_P}$, and its dual space as $T^*_{\mathcal{S}_P}$. Unit basis vectors of $T_{\mathcal{S}_P}$ are denoted as $\mathbf{e}_i$, and dual-basis 1-forms of $T^*_{\mathcal{S}_P}$ are denoted as $\boldsymbol{\eta}^i$. In the case of an orthonormal basis for $T_{\mathcal{S}_P}$, the associated dual-basis 1-forms are specifically labeled as $\boldsymbol{\theta}^i$. The exterior derivative operator on forms is denoted by $\mathbf{d}$, and the wedge product of forms is denoted by $\wedge$.

Throughout the text, all quantities defined on a curve C or a surface $\mathcal{S}$, including scalars, vectors, and forms, are assumed to be smooth functions of the corresponding point P. This dependence is omitted for conciseness.

2.2 Curves: The Frenet-Serret frame

Let $C = P(s)$ be a curve parameterized by a unit-speed parameter s, ensuring then $\|P'\| = 1$, where prime indicates differentiation with respect to s. At each point P of this curve, the *unit tangent* vector $\mathbf{t}$ is defined as $\mathbf{t} = P'$. We proceed by defining a second unit vector $\mathbf{n}$, called the *principal normal*, as $\mathbf{n} = \mathbf{t}'/\|\mathbf{t}'\|$. Since the vector $\mathbf{t}$ is unitary, it shall be orthogonal to the vector $\mathbf{n}$. Finally, we define a third unit vector $\mathbf{b}$ as $\mathbf{b} = \mathbf{t} \times \mathbf{n}$, called the *binormal*. In this way, at each point P, we establish the orthonormal frame $(\mathbf{t}, \mathbf{n}, \mathbf{b})$, commonly known as the *Frenet-Serret frame*.

At each point P, the quantity $\kappa = \|\mathbf{t}'\|$ is called the *curvature*, representing the rotation rate of the vector $\mathbf{t}$ towards $\mathbf{n}$ as the point P moves along the curve at unit speed. By symmetry, the vector $\mathbf{n}$ rotates toward $\mathbf{t}$ with rate $-\kappa$. The rotation rate of the vector $\mathbf{n}$ towards the binormal $\mathbf{b}$ is called the *torsion* and is denoted as τ. Since the rotation of $\mathbf{t}$ is null towards $\mathbf{b}$, by symmetry we get $\tau = -\|\mathbf{b}'\|$. Summarizing, we have:

$$\mathbf{t}' = \kappa\,\mathbf{n}, \quad \mathbf{n}' = -\kappa\,\mathbf{t} + \tau\,\mathbf{b}, \quad \mathbf{b}' = -\tau\,\mathbf{n}. \tag{2.1}$$

Let us now introduce a dual-basis $\mathbf{d}s$ in the tangent line of the curve at P, such that $\mathbf{d}s(\mathbf{t}) = 1$. We can now define the exterior derivative of the point P as $\mathbf{d}P = P'\mathbf{d}s$, resulting in a vector where each component is the exterior derivative of the corresponding component of P. Similarly, we can define the exterior derivatives of the Frenet-Serret frame as:

$$\mathbf{dt} = \mathbf{t}'\mathbf{d}s, \quad \mathbf{dn} = \mathbf{n}'\mathbf{d}s, \quad \mathbf{db} = \mathbf{b}'\mathbf{d}s. \tag{2.2}$$

Consider now a generic curve parametrization $C = P(r)$. Let then $\mathbf{d}r$ be the dual-basis of P', such that $\mathbf{d}r(P') = 1$. To recover the geometric quantities given by a unit-speed parametrization, we can compute the unit tangent vector as $\mathbf{t} = P'/\|P'\|$, and introduce the dual-basis 1-form $\boldsymbol{\theta}$ associated with $\mathbf{t}$, such that $\boldsymbol{\theta}(\mathbf{t}) = 1$. This is achieved by setting $\boldsymbol{\theta} = \|P'\|\,\mathbf{d}r$. Conceptually, the 1-form $\boldsymbol{\theta}$ acts as a 'ruler', measuring the length of a vector tangent to the curve. From Equations 2.1 and 2.2, we can express the exterior derivatives of the Frenet-Serret frame in matrix form, without considering a specific parametrization, as:

$$\begin{pmatrix} \mathbf{dt} \\ \mathbf{dn} \\ \mathbf{db} \end{pmatrix} = \begin{pmatrix} 0 & \kappa\,\boldsymbol{\theta} & 0 \\ -\kappa\,\boldsymbol{\theta} & 0 & \tau\,\boldsymbol{\theta} \\ 0 & -\tau\,\boldsymbol{\theta} & 0 \end{pmatrix} \begin{pmatrix} \mathbf{t} \\ \mathbf{n} \\ \mathbf{b} \end{pmatrix}. \tag{2.3}$$

2.3 Curves on surfaces: The Darboux frame

Now, consider a curve C embedded in a surface $\mathcal{S}$. At every point P along this curve, the tangent vector $\mathbf{t}$ naturally lies in the tangent plane $T_{\mathcal{S}_P}$. We can then construct a new frame $(\mathbf{e}_1, \mathbf{e}_2, \mathbf{e}_n)$, called the *Darboux frame*, as follows: Let $\mathbf{e}_1$ coincide with the tangent vector $\mathbf{t}$, define $\mathbf{e}_2$ as the unit vector obtained by rotating $\mathbf{e}_1$ counterclockwise by 90° in the tangent plane $T_{\mathcal{S}_P}$, and set $\mathbf{e}_n$ as the surface normal given by $\mathbf{e}_n = \mathbf{e}_1 \times \mathbf{e}_2$, as illustrated in Figure 5.

The set $\{\mathbf{e}_1, \mathbf{e}_2\}$ forms an orthonormal basis of $T_{\mathcal{S}_P}$. Let $\{\boldsymbol{\theta}^1, \boldsymbol{\theta}^2\}$ represent the corresponding dual-basis of $T^*_{\mathcal{S}_P}$. Notably, $\boldsymbol{\theta}^1(\mathbf{t}) = 1$. Thus, we can express the exterior derivatives of Equation 2.3 by substituting $\boldsymbol{\theta}$ with $\boldsymbol{\theta}^1$. It's essential to note that all quantities are here defined solely along the curve C.

Let ϕ denote the angle that aligns the vectors $\mathbf{n}$ and $\mathbf{e}_2$ through a rotation around $\mathbf{t}$ (see Figure 5). Then, we have:

$$\mathbf{e}_2 = \cos\phi\,\mathbf{n} + \sin\phi\,\mathbf{b}, \quad \text{and} \quad \mathbf{e}_n = -\sin\phi\,\mathbf{n} + \cos\phi\,\mathbf{b}. \tag{2.4}$$

By taking the exterior derivatives of the Darboux frame and utilizing relations 2.4 alongside the Frenet-Serret equations 2.3, we obtain:

$$\begin{pmatrix} \mathbf{de}_1 \\ \mathbf{de}_2 \\ \mathbf{de}_n \end{pmatrix} = \begin{pmatrix} 0 & g\,\boldsymbol{\theta}^1 & n\,\boldsymbol{\theta}^1 \\ -g\,\boldsymbol{\theta}^1 & 0 & t\,\boldsymbol{\theta}^1 \\ -n\,\boldsymbol{\theta}^1 & -t\,\boldsymbol{\theta}^1 & 0 \end{pmatrix} \begin{pmatrix} \mathbf{e}_1 \\ \mathbf{e}_2 \\ \mathbf{e}_n \end{pmatrix}, \tag{2.5}$$

with

$$n = -\kappa \sin\phi, \tag{2.6}$$
$$g = \kappa \cos\phi, \tag{2.7}$$
$$t = \tau + \mathbf{d}\phi(\mathbf{e}_1). \tag{2.8}$$

Here, n, g, and t are respectively termed the *normal curvature*, the *geodesic curvature*, and the *geodesic torsion* of the curve C with respect to the surface $\mathcal{S}$.

At a point P of $\mathcal{S}$, the extreme values that the normal curvature n of a curve passing through P can attain are called *principal curvatures*, denoted as κ_I, κ_{II}. It can be shown [do Carmo 1976] that these two values occur along two orthogonal tangent directions, called *principal curvature directions*. Let then β be the angle that a curve tangent vector $\mathbf{e}_1$ makes with the principal curvature direction corresponding to κ_I. *Euler's formulas* state that:

$$\begin{aligned} n &= \kappa_I \cos^2\beta + \kappa_{II} \sin^2\beta, \\ t &= (\kappa_I - \kappa_{II}) \sin\beta \cos\beta. \end{aligned} \tag{2.9}$$

The product of principal curvatures $K = \kappa_I \kappa_{II}$ is called the *Gaussian curvature* of the surface. Their mean value $H = (\kappa_I + \kappa_{II})/2$ is called *mean curvature*.

The vanishing of one of the relative curvatures n, g, and t, defines three distinct types of special curves that exist on surfaces:

Definition 1. *An* asymptotic curve *is a surface curve where $n = 0$, or equivalently $\phi = 0$.*

Since their curvature in the normal direction vanishes, along asymptotic curves it is possible to dispose a straight lamella orthogonally to the surface $\mathcal{S}$, as shown if Figure 6 *left*.

Definition 2. *A* geodesic curve *is a surface curve where $g = 0$, or equivalently $\phi = \pm\pi/2$.*

In this case, the curve has vanishing curvature in the surface tangent plane, and it is possible to dispose along it a straight lamella oriented tangentially to the surface, as shown in Figure 6 *center*.

Definition 3. *A* principal curvature line *is a surface curve where $t = 0$. For such a curve, the normal curvature n coincides with one of the two principal curvatures κ_I, κ_{II}.*

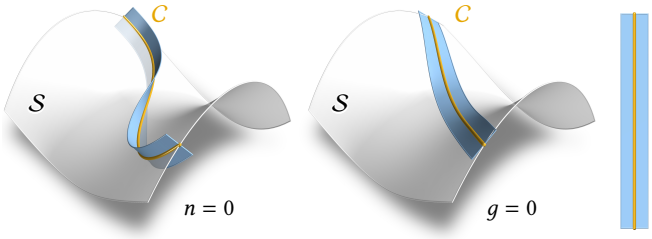

Fig. 6. On the *left*: Along an asymptotic curve, it is possible to dispose the straight lamella shown on the *right* perpendicular to the surface. In the *center*: Along a geodesic curve, the straight lamella can be disposed tangentially to the surface.

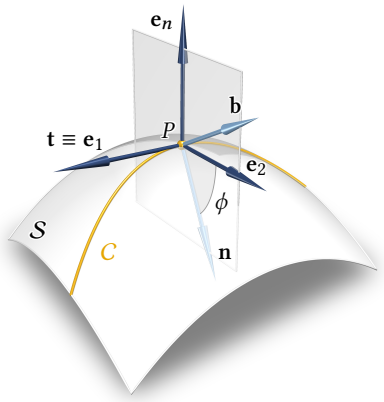

Fig. 5. Frenet-Serret frame $(\mathbf{t}, \mathbf{n}, \mathbf{b})$ and Darboux frame $(\mathbf{e}_1, \mathbf{e}_2, \mathbf{e}_n)$ of a curve C at a point P on a surface $\mathcal{S}$. The two frames are aligned by a rotation ϕ around the vector $\mathbf{t} \equiv \mathbf{e}_1$.

2.4 Orthogonal curve nets: The Cartan frame

Let C^1 and C^2 denote two families of curves covering a surface $\mathcal{S}$, mutually orthogonal at each point P on $\mathcal{S}$. At every point P, construct a positively oriented orthonormal frame $(\mathbf{e}_1, \mathbf{e}_2, \mathbf{e}_n)$, where $\mathbf{e}_1$ and $\mathbf{e}_2$ represent the unit tangent vectors of curves C^1 and C^2, respectively, and $\mathbf{e}_n$ is the unit surface normal. Ensure that, at each point, the tangents to the curves maintain consistent orientation for both families C^1 and C^2 across the entire surface $\mathcal{S}$. By construction, the frame $(\mathbf{e}_1, \mathbf{e}_2, \mathbf{e}_n)$ forms the Darboux frame for curves C^1, while the frame $(\mathbf{e}_2, -\mathbf{e}_1, \mathbf{e}_n)$ constitutes the Darboux frame for curves C^2. The set $\{\mathbf{e}_1, \mathbf{e}_2\}$ serves as an orthonormal basis for the tangent plane $T_{\mathcal{S}_P}$. Let $\{\boldsymbol{\theta}^1, \boldsymbol{\theta}^2\}$ denote the corresponding dual-basis.

At each point P, we now encounter two curves, each belonging to either C^1 or C^2. The dual-basis 1-forms $\boldsymbol{\theta}^1$ and $\boldsymbol{\theta}^2$ now measure the

lengths of tangent vectors belonging to $T_{\mathcal{S}_P}$ along the corresponding curve tangent. This also enables us to represent the rotation of the Darboux frame along every direction of $T_{\mathcal{S}_P}$ by summing the contributions in the two curve directions $\mathbf{e}_1$ and $\mathbf{e}_2$. Writing Equations 2.5 for both curves, and considering the inversion of the Darboux frame for the curve from C^2, we can express the rotation of the Darboux frame as follows:

$$\begin{pmatrix} \mathbf{de}_1 \\ \mathbf{de}_2 \\ \mathbf{de}_n \end{pmatrix} = \begin{pmatrix} 0 & g_1\boldsymbol{\theta}^1 + g_2\boldsymbol{\theta}^2 & n_1\boldsymbol{\theta}^1 - t_2\boldsymbol{\theta}^2 \\ -g_1\boldsymbol{\theta}^1 - g_2\boldsymbol{\theta}^2 & 0 & t_1\boldsymbol{\theta}^1 + n_2\boldsymbol{\theta}^2 \\ -n_1\boldsymbol{\theta}^1 + t_2\boldsymbol{\theta}^2 & -t_1\boldsymbol{\theta}^1 - n_2\boldsymbol{\theta}^2 & 0 \end{pmatrix} \begin{pmatrix} \mathbf{e}_1 \\ \mathbf{e}_2 \\ \mathbf{e}_n \end{pmatrix}, \tag{2.10}$$

where n_1, g_1, and t_1 represent respectively the normal curvature, the geodesic curvature, and the geodesic torsion of the curve from C^1. Similarly, n_2, g_2, and t_2 denote the same quantities for the curve from C^2. Equations 2.10 can be concisely written as follows:

$$\begin{pmatrix} \mathbf{de}_1 \\ \mathbf{de}_2 \\ \mathbf{de}_n \end{pmatrix} = \begin{pmatrix} 0 & \boldsymbol{\omega}_{12} & \boldsymbol{\omega}_{1n} \\ \boldsymbol{\omega}_{21} & 0 & \boldsymbol{\omega}_{2n} \\ \boldsymbol{\omega}_{n1} & \boldsymbol{\omega}_{n2} & 0 \end{pmatrix} \begin{pmatrix} \mathbf{e}_1 \\ \mathbf{e}_2 \\ \mathbf{e}_n \end{pmatrix}, \tag{2.11}$$

where $\boldsymbol{\omega}_{ij}$ are called the *connection forms* of the curve net, with $i, j \in \{1, 2, n\}$, and where $\boldsymbol{\omega}_{ij} = -\boldsymbol{\omega}_{ji}$. The connection form $\boldsymbol{\omega}_{ij}(\mathbf{v})$ expresses the initial rotation rate at which $\mathbf{e}_i$ rotates toward $\mathbf{e}_j$ as P moves with velocity $\mathbf{v}$.

Consider now the second Euler's equation 2.9. Let β_1 and β_2 denote the angles that vectors $\mathbf{e}_1$ and $\mathbf{e}_2$ form with the first principal curvature direction. Since $\beta_1 - \beta_2 = \pm\pi/2$, it follows $t_1 = -t_2$. Therefore, we can express the connection forms as:

$$\begin{aligned} \boldsymbol{\omega}_{12} &= g_1\boldsymbol{\theta}^1 + g_2\boldsymbol{\theta}^2, \\ \boldsymbol{\omega}_{1n} &= n_1\boldsymbol{\theta}^1 + t_1\boldsymbol{\theta}^2, \\ \boldsymbol{\omega}_{2n} &= t_1\boldsymbol{\theta}^1 + n_2\boldsymbol{\theta}^2. \end{aligned} \tag{2.12}$$

We aim now to express the exterior derivatives of connection and dual-basis forms. Considering that the exterior derivative of the position vector P can be represented in the frame basis as $\mathbf{d}P = \mathbf{e}_1\boldsymbol{\theta}^1 + \mathbf{e}_2\boldsymbol{\theta}^2$, setting $\mathbf{dd}P = 0$, and using Equations 2.11, yields the first set of Cartan's structural equations:

$$\begin{aligned} \mathbf{d}\boldsymbol{\theta}^1 &= \boldsymbol{\omega}_{12} \wedge \boldsymbol{\theta}^2 = g_1\, \boldsymbol{\theta}^1 \wedge \boldsymbol{\theta}^2, \\ \mathbf{d}\boldsymbol{\theta}^2 &= \boldsymbol{\omega}_{21} \wedge \boldsymbol{\theta}^1 = g_2\, \boldsymbol{\theta}^1 \wedge \boldsymbol{\theta}^2. \end{aligned} \tag{2.13}$$

Similarly, enforcing $\mathbf{dde}_i = 0, i \in \{1, 2, n\}$, leads to the second set of Cartan's structural equations:

$$\begin{aligned} \mathbf{d}\boldsymbol{\omega}_{12} &= \boldsymbol{\omega}_{1n} \wedge \boldsymbol{\omega}_{n2} = (t_1^2 - n_1 n_2)\, \boldsymbol{\theta}^1 \wedge \boldsymbol{\theta}^2 \\ \mathbf{d}\boldsymbol{\omega}_{1n} &= \boldsymbol{\omega}_{12} \wedge \boldsymbol{\omega}_{2n} = (g_1 n_2 - g_2 t_1)\, \boldsymbol{\theta}^1 \wedge \boldsymbol{\theta}^2, \\ \mathbf{d}\boldsymbol{\omega}_{2n} &= \boldsymbol{\omega}_{21} \wedge \boldsymbol{\omega}_{1n} = (g_2 n_1 - g_1 t_1)\, \boldsymbol{\theta}^1 \wedge \boldsymbol{\theta}^2. \end{aligned} \tag{2.14}$$

Form Euler's equations 2.9, we observe that the first Equation 2.14 tells us that

$$\mathbf{d}\boldsymbol{\omega}_{12} = -K\, \boldsymbol{\theta}^1 \wedge \boldsymbol{\theta}^2, \tag{2.15}$$

where K is the Gaussian curvature of the surface $\mathcal{S}$ at P. This equivalence is also known as the *Gauss equation* of the surface. The last two Equations 2.14 are the so-called *Mainardi-Codazzi equations*. By taking the exterior derivatives of the connection forms as outlined in Equations 2.12, substituting Equations 2.13, and evaluating the 2-forms on $\mathbf{e}_1, \mathbf{e}_2$, the Mainardi-Codazzi equations become:

$$\begin{aligned} \mathbf{d}t_1(\mathbf{e}_1) - \mathbf{d}n_1(\mathbf{e}_2) &= g_1(n_2 - n_1) - 2g_2 t_1, \\ \mathbf{d}n_2(\mathbf{e}_1) - \mathbf{d}t_1(\mathbf{e}_2) &= g_2(n_1 - n_2) - 2g_1 t_1. \end{aligned} \tag{2.16}$$

2.5 Non-orthogonal curve nets: The double frame

Let C^1 and C^3 be two families of curves covering a surface $\mathcal{S}$. To handle a non-orthogonal curve net, let us introduce two additional curve families, C^2 and C^4, running orthogonally to C^1 and C^3, respectively. At each point P of $\mathcal{S}$, construct two orthonormal frames $(\mathbf{e}_1, \mathbf{e}_2, \mathbf{e}_n)$ and $(\mathbf{e}_3, \mathbf{e}_4, \mathbf{e}_n)$, with a positive orientation, where $\mathbf{e}_1$, $\mathbf{e}_2$, $\mathbf{e}_3$, $\mathbf{e}_4$ are the unit tangent vectors of the curves C^1, C^2, C^3, C^4 respectively, and $\mathbf{e}_n$ is the unit surface normal, as shown in Figure 7. We call this pair of frames a *double frame*.

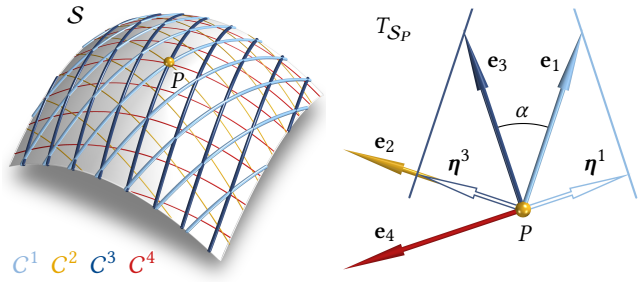

Fig. 7. On the *left*: Non-orthogonal curve net composed of curves C^1 and C^3, together with the respectively orthogonal curves C^2 and C^4. On the *right*: The corresponding double frame at a point P.

At each point P, both sets $\{\mathbf{e}_1, \mathbf{e}_2\}$ and $\{\mathbf{e}_3, \mathbf{e}_4\}$ serve as orthonormal bases of $T_{\mathcal{S}_P}$, with corresponding dual-bases denoted as $\{\boldsymbol{\theta}^1, \boldsymbol{\theta}^2\}$ and $\{\boldsymbol{\theta}^3, \boldsymbol{\theta}^4\}$. The set $\{\mathbf{e}_1, \mathbf{e}_3\}$ constitutes a non-orthogonal, unit-length basis for $T_{\mathcal{S}_P}$, with the resulting dual-basis denoted as $\{\boldsymbol{\eta}^1, \boldsymbol{\eta}^3\}$ (See figure 7). If α is the angle between $\mathbf{e}_1$ and $\mathbf{e}_3$ (positive counter-clockwise), we can express:

$$\begin{aligned} \mathbf{e}_1 &= \cos\alpha\, \mathbf{e}_3 - \sin\alpha\, \mathbf{e}_4, \\ \mathbf{e}_3 &= \cos\alpha\, \mathbf{e}_1 + \sin\alpha\, \mathbf{e}_2. \end{aligned} \tag{2.17}$$

Hence, we obtain $\boldsymbol{\theta}^1(\mathbf{e}_3) = \boldsymbol{\theta}^3(\mathbf{e}_1) = \cos\alpha$, $\boldsymbol{\theta}^2(\mathbf{e}_3) = \sin\alpha$, and $\boldsymbol{\theta}^4(\mathbf{e}_1) = -\sin\alpha$. Utilizing the dual-basis equations A.1, we obtain:

$$\begin{aligned} \boldsymbol{\theta}^1 &= \boldsymbol{\eta}^1 + \cos\alpha\, \boldsymbol{\eta}^3, \quad \boldsymbol{\theta}^2 = \sin\alpha\, \boldsymbol{\eta}^3, \\ \boldsymbol{\theta}^3 &= \cos\alpha\, \boldsymbol{\eta}^1 + \boldsymbol{\eta}^3, \quad \boldsymbol{\theta}^4 = -\sin\alpha\, \boldsymbol{\eta}^1. \end{aligned} \tag{2.18}$$

It follows that

$$\boldsymbol{\theta}^1 \wedge \boldsymbol{\theta}^2 = \boldsymbol{\theta}^3 \wedge \boldsymbol{\theta}^4 = \sin\alpha\, \boldsymbol{\eta}^1 \wedge \boldsymbol{\eta}^3. \tag{2.19}$$

Now, the frames $(\mathbf{e}_1, \mathbf{e}_2, \mathbf{e}_n)$ and $(\mathbf{e}_3, \mathbf{e}_4, \mathbf{e}_n)$ give rise to six connection forms, as in Equations 2.12, three for each frame. In particular, the connection form $\boldsymbol{\omega}_{34}$ equals the connection form $\boldsymbol{\omega}_{12}$ plus their relative rotation expressed by $\mathbf{d}\alpha$, and vice versa. Therefore,

$$\boldsymbol{\omega}_{34} = \boldsymbol{\omega}_{12} + \mathbf{d}\alpha, \quad \boldsymbol{\omega}_{12} = \boldsymbol{\omega}_{34} - \mathbf{d}\alpha, \tag{2.20}$$

(a proof can be found in [O'Neill 2006] p.325). By considering that $g_1 = \boldsymbol{\omega}_{12}(\mathbf{e}_1)$ and $g_3 = \boldsymbol{\omega}_{34}(\mathbf{e}_3)$, plugging Equations 2.17 into Equations 2.20, we obtain:

$$\begin{aligned} g_1 &= \boldsymbol{\omega}_{34}(\mathbf{e}_1) - \mathbf{d}\alpha(\mathbf{e}_1) = g_3 \cos\alpha - g_4 \sin\alpha - \mathbf{d}\alpha(\mathbf{e}_1), \\ g_3 &= \boldsymbol{\omega}_{12}(\mathbf{e}_3) + \mathbf{d}\alpha(\mathbf{e}_3) = g_1 \cos\alpha + g_2 \sin\alpha + \mathbf{d}\alpha(\mathbf{e}_3). \end{aligned} \tag{2.21}$$

2.6 Derivatives of functions along curve nets

The connection forms of Equations 2.12 encapsulate in their components the curvature information of the net curves. These components are scalar functions defined on the net surface $\mathcal{S}$. We analyze now the variation of scalar functions along a curve net, a crucial aspect for our subsequent investigations.

Consider a generic curve net $\{C^1, C^3\}$ on a surface $\mathcal{S}$, along with a basis $\{\mathbf{e}_1, \mathbf{e}_3\}$ of $T_{\mathcal{S}_P}$, defined by their respective unit tangent vectors, and the corresponding dual-basis $\{\boldsymbol{\eta}^1, \boldsymbol{\eta}^3\}$. For conciseness, let $(i, j) = (1, 3)$ or $(3, 1)$.

Proposition 1. *Let $\boldsymbol{\nu} = \nu_1\boldsymbol{\eta}^1 + \nu_3\boldsymbol{\eta}^3$ be a 1-form on $\mathcal{S}$ at point P. Then, $\boldsymbol{\nu} \wedge \boldsymbol{\eta}^i = 0$ if and only if $\nu_j = 0$.*

Proof. We have $\boldsymbol{\nu} \wedge \boldsymbol{\eta}^i = \nu_j\, \boldsymbol{\eta}^j \wedge \boldsymbol{\eta}^i$. For non-degenerate nets, the 2-form $\boldsymbol{\eta}^j \wedge \boldsymbol{\eta}^i$ never vanishes. □

Proposition 2. *Let f be a scalar function on $\mathcal{S}$. Then, $\mathbf{d}f \wedge \boldsymbol{\eta}^i = 0$ for all points $P \in \mathcal{S}$ if and only if the function f is constant along curves C^j.*

Proof. By definition of exterior derivative, the derivative of a function f along the direction $\mathbf{e}_j$ is given by $\mathbf{d}f(\mathbf{e}_j)$. Proposition 1 implies here $\mathbf{d}f(\mathbf{e}_j) = 0$. Since $\mathbf{e}_j$ is the tangent vector of curves C^j, we conclude that the function f remains constant along these curves. □

Proposition 3. *Let f and h be scalar functions on $\mathcal{S}$. If $\mathbf{d}f = h\boldsymbol{\eta}^i$ and $\mathbf{d}\boldsymbol{\eta}^i = 0$ for all points $P \in \mathcal{S}$, then both functions f and h are constant along curves C_j.*

Proof. We have $\mathbf{d}\mathbf{d}f = \mathbf{d}h \wedge \boldsymbol{\eta}^i + h\,\mathbf{d}\boldsymbol{\eta}^i$. Since $\mathbf{d}\mathbf{d}f = 0$ by definition of exterior derivative, $\mathbf{d}\boldsymbol{\eta}^i = 0$ implies $\mathbf{d}h \wedge \boldsymbol{\eta}^i = 0$. Also, for Proposition 1, $\mathbf{d}f = h\boldsymbol{\eta}^i$ implies $\mathbf{d}f \wedge \boldsymbol{\eta}^i = 0$. Proposition 2 yields the result. □

Proposition 4. *Let f be a scalar function on $\mathcal{S}$. Then, $\mathbf{d}f(\mathbf{e}_1) = \mathbf{d}f(\mathbf{e}_3)$ for all points $P \in \mathcal{S}$ if and only if the function f is constant along a family of bisecting curves of C^1 and C^3 tangent to $\mathbf{e}_1 - \mathbf{e}_3$.*

Proof. From linearity of 1-forms, we have $\mathbf{d}f(\mathbf{e}_1) - \mathbf{d}f(\mathbf{e}_3) = \mathbf{d}f(\mathbf{e}_1 - \mathbf{e}_3) = 0$, indicating that the function f remains constant along the direction $\mathbf{e}_1 - \mathbf{e}_3$. Since both $\mathbf{e}_1$ and $\mathbf{e}_3$ are unit vectors, the direction $\mathbf{e}_1 - \mathbf{e}_3$ is a bisecting direction of the net. □

3 ALIGNABLE NETS

This section explores the design principles behind alignable lamella gridshells through the study of alignable nets. For this purpose, consider a generic curve net $\{C^1, C^3\}$ on a surface $\mathcal{S}$. At each point $P \in \mathcal{S}$, let $\mathbf{e}_1$ and $\mathbf{e}_3$ represent their respective tangent vectors. From this net, we can construct a *gridshell* by selecting a finite number of curves from both families C^1 and C^3. These curves intersect at a finite number of *joints*, where the tangent vectors $\mathbf{e}_1$ and $\mathbf{e}_3$ form an angle α.

A gridshell is considered *alignable* if, by closing the angle α at each joint, it smoothly collapses into a planar curve without changing the lengths of the curve segments between joints. In a general case, during this transformation, the curves are considered 'flexible', meaning they can change their curvature κ and their torsion τ. Throughout the alignment process, the surface $\mathcal{S}$ undergoes transformation, along with changes in the normal curvature n and geodesic curvature g of the curves relative to the transformed surface.

To design alignable lamella gridshells, we will explore alignable nets that preserve either the relative curvature g or n during the alignment process, as detailed in Section 2. In this scenario, curves can be materialized using planar lamellae arranged either tangentially or orthogonally to the surface $\mathcal{S}$.

Hereafter, we first identify the necessary properties for a curve net to yield an alignable gridshell. Then, we utilize the double frame introduced in Section 2.5 to investigate the geometric prerequisites for a surface to allow the existence of a curve net with vanishing geodesic curvature g or constrained normal curvature n.

3.1 Lengths of net curves

Let $\{C^1, C^3\}$ be a generic curve net on a surface $\mathcal{S}$, with unit tangent vectors forming a basis $\{\mathbf{e}_1, \mathbf{e}_3\}$ of $T_{\mathcal{S}_P}$ along with a dual-basis $\{\boldsymbol{\eta}^1, \boldsymbol{\eta}^3\}$, as illustrated in Section 2.5. Choose a specific curve of the net, and consider the segment between two points A and B, both lying on the curve. Let us denote this oriented segment as C^i_{AB}, where $i = 1, 3$ indicates the curve family to which the curve belongs to. We say that the segment C^i_{AB} is *positively oriented* if it is oriented in the same direction of its tangent vector $\mathbf{e}_i$. Our objective is to determine the length of the segment, denoted as ℓ^i_{AB}. To this end, we observe that, at each point $P \in \mathcal{S}$, the dual-basis 1-form $\boldsymbol{\eta}^i$ measure the component of a tangent vector of $T_{\mathcal{S}_P}$ along the unit basis vector $\mathbf{e}_i$, and therefore the length of every vector tangent to a curve C^i. According to Equation A.3, if the segment C^i_{AB} is positively oriented, we can then express its length as:

$$\ell^i_{AB} = \int_{C^i_{AB}} \boldsymbol{\eta}^i = -\int_{C^i_{BA}} \boldsymbol{\eta}^i. \tag{3.1}$$

Let $(i, j) = (1, 3)$ or $(3, 1)$. We also observe that

$$\int_{C^i_{AB}} \boldsymbol{\eta}^j = 0. \tag{3.2}$$

3.2 Alignability of curve nets

In a curve net $\{C^1, C^3\}$, select four curves, two from each family. Let $\mathcal{R}$ be the quadrilateral surface region $\mathcal{R}$ bounded by the four curves, with corners A, B, C, and D as shown in Figure 8. Let then

$\partial\mathcal{R}$ be the boundary of the region $\mathcal{R}$, composed by curve segments $C^1_{AB}, C^3_{BC}, C^1_{CD}, C^3_{DA}$. We call such a union of curves $\partial\mathcal{R}$ a *net-loop*.

Definition 4. *A net-loop $\partial\mathcal{R}$ is* alignable *if $\ell^1_{AB}+\ell^3_{BC} = \ell^3_{AD}+\ell^1_{DC}$. A curve net is alignable if all of its net-loops are alignable.*

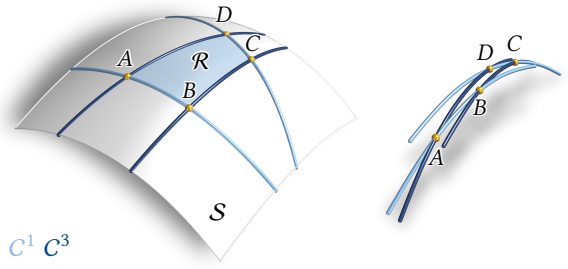

Fig. 8. Alignable net-loop. On the *left*: A net-loop $\partial\mathcal{R}$ between joints A, B, C, and D bounding a surface region $\mathcal{R}$. On the *right*: Aligned net-loop. The alignment requires $\ell^1_{AB} + \ell^3_{BC} = \ell^3_{AD} + \ell^1_{DC}$.

If a curve net is alignable, it follows that all gridshells extracted from the net will also be alignable. We look now into the condition for a curve net to be alignable. To this end, let $\mathbf{e}_1$, $\mathbf{e}_3$ be the unit tangent vectors of curves C^1, C^3, with dual-basis $\{\boldsymbol{\eta}^1, \boldsymbol{\eta}^3\}$. Then:

Proposition 5. *A curve net on a surface $\mathcal{S}$ is alignable if and only if, at all points $P \in \mathcal{S}$,*

$$\mathbf{d}\boldsymbol{\eta}^1 + \mathbf{d}\boldsymbol{\eta}^3 = 0.$$

Proof. Let us consider a net-loop $\partial\mathcal{R}$, oriented in direction $ABCD$, with C^1_{AB} and C^3_{BC} positively oriented. According to Equations 3.1 and 3.2, we have:

$$\ell^1_{AB} - \ell^1_{DC} = \int_{\partial\mathcal{R}} \boldsymbol{\eta}^1 \quad \text{and} \quad \ell^3_{BC} - \ell^3_{AD} = \int_{\partial\mathcal{R}} \boldsymbol{\eta}^3.$$

Applying Stokes' theorem and imposing the alignability condition of Definition 4, yields:

$$\int_{\partial\mathcal{R}} \boldsymbol{\eta}^1 + \boldsymbol{\eta}^3 = \int_{\mathcal{R}} \mathbf{d}\boldsymbol{\eta}^1 + \mathbf{d}\boldsymbol{\eta}^3 = 0, \quad \text{for all net-loops } \partial\mathcal{R}. \tag{3.3}$$

The last equality holds for all net-loops $\partial\mathcal{R}$ if $\mathbf{d}\boldsymbol{\eta}^1 + \mathbf{d}\boldsymbol{\eta}^3 = 0$ at all points $P \in \mathcal{S}$. Proposition 8 in Appendix B shows that this condition is not only sufficient but also necessary. □

We now establish a second condition for the alignability of the curve net, one that incorporates the geodesic curvatures of the curves and the angle between them:

Proposition 6. *Consider a curve net $\{C^1, C^3\}$ on a surface $\mathcal{S}$. At each point $P \in \mathcal{S}$, let g_1 and g_3 denote the geodesic curvatures of the curves passing through that point, and $\mathbf{e}_1$ and $\mathbf{e}_3$ be their respective tangent vectors, forming an angle α. The curve net is alignable if and only if, at every point P,*

$$\mathbf{d}\alpha(\mathbf{e}_1) + g_1 = \mathbf{d}\alpha(\mathbf{e}_3) - g_3. \tag{3.4}$$

Proof. Consider a double frame associated with the curve net, as detailed in Section 2.5. By computing the exterior derivatives of $\boldsymbol{\theta}^1$ and $\boldsymbol{\theta}^3$ from Equations 2.18, we get:

$$\begin{aligned} \mathbf{d}\boldsymbol{\theta}^1 &= \mathbf{d}\boldsymbol{\eta}^1 + \cos\alpha\, \mathbf{d}\boldsymbol{\eta}^3 - \sin\alpha\, \mathbf{d}\alpha \wedge \boldsymbol{\eta}^3, \\ \mathbf{d}\boldsymbol{\theta}^3 &= \mathbf{d}\boldsymbol{\eta}^3 + \cos\alpha\, \mathbf{d}\boldsymbol{\eta}^1 - \sin\alpha\, \mathbf{d}\alpha \wedge \boldsymbol{\eta}^1. \end{aligned} \tag{3.5}$$

Consider now the first Cartan structural equations 2.13. Using Equation 2.19, we can write:

$$\mathbf{d}\boldsymbol{\theta}^1 = g_1 \sin\alpha\, \boldsymbol{\eta}^1 \wedge \boldsymbol{\eta}^3 \quad \text{and} \quad \mathbf{d}\boldsymbol{\theta}^3 = g_3 \sin\alpha\, \boldsymbol{\eta}^1 \wedge \boldsymbol{\eta}^3. \tag{3.6}$$

Next, summing Equations 3.5 and considering that

$$\mathbf{d}\alpha \wedge \boldsymbol{\eta}^3 = \mathbf{d}\alpha(\mathbf{e}_1)\, \boldsymbol{\eta}^1 \wedge \boldsymbol{\eta}^3, \quad \mathbf{d}\alpha \wedge \boldsymbol{\eta}^1 = -\mathbf{d}\alpha(\mathbf{e}_3)\, \boldsymbol{\eta}^1 \wedge \boldsymbol{\eta}^3,$$

by substituting Equations 3.6 we find:

$$(g_1 + g_3 + \mathbf{d}\alpha(\mathbf{e}_1) - \mathbf{d}\alpha(\mathbf{e}_3))\, \boldsymbol{\eta}^1 \wedge \boldsymbol{\eta}^3 = \cot\frac{\alpha}{2}(\mathbf{d}\boldsymbol{\eta}^1 + \mathbf{d}\boldsymbol{\eta}^3).$$

Since, for non-degenerate nets, both $\boldsymbol{\eta}^1 \wedge \boldsymbol{\eta}^3$ and α never vanish, this yields the desired result. □

Consider now a Chebyshev net, which is an alignable net where all lengths of curves segments are equal. In this case, we can state that:

Definition 5. *A* Chebyshev net *is a net where, for all net-loops, $\ell^1_{AB} = \ell^1_{CD}$ and $\ell^2_{AD} = \ell^2_{BC}$.*

Proposition 7. *A curve net $\{C^1, C^3\}$ on a surface $\mathcal{S}$ is a Chebyshev net if and only if, at all points $P \in \mathcal{S}$,*

$$\mathbf{d}\boldsymbol{\eta}^1 = 0 \quad \textit{and} \quad \mathbf{d}\boldsymbol{\eta}^3 = 0.$$

Moreover, being g_1 and g_3 the geodesic curvatures of the curves of the net, and α the angle between them, it holds

$$g_1 = -\mathbf{d}\alpha(\mathbf{e}_1) \quad \textit{and} \quad g_3 = \mathbf{d}\alpha(\mathbf{e}_3). \tag{3.7}$$

Proof. It follows from the proof of Proposition 5 and from Equations 3.5. □

Propositions 6 and 7 provide insights into the degrees of freedom involved in constructing alignable and Chebyshev nets: On a surface $\mathcal{S}$, trace two arbitrary curves C^1_0 and C^3_0 from a point P. In case of a Chebyshev net, according to Equation 3.7, the angle α along the curves C^1_0 and C^3_0 is now determined by integrating their geodesic curvatures g_1 and g_3 starting from P. These angles α now determine the geodesic curvatures of all curves C^1 at intersection with the curve C^3_0 and vice versa. With Equation 3.7 we can then integrate the full net. In case of an alignable net, Equation 3.4 indicates that there remains the freedom to choose the angle α along one family of curves. This means that the net is determined by an arbitrary family of curves and a single arbitrary curve from the other family.

3.3 Geodesic alignable nets

In this section, we investigate alignable nets where both families of curves C^1 and C^3 are geodesics. In this case, the net allows the extraction of a gridshell where curves can be materialized with straight lamellae arranged tangentially to the net surface $\mathcal{S}$. However, this condition imposes a restriction on the shape of the surface $\mathcal{S}$. In particular:

Theorem 1. *A geodesic alignable net exists only and on all surfaces that can be isometrically mapped to surfaces of revolution. There, the net is symmetric to curves that map to meridians under the isometry. Additionally, the angle between curves of the net is constant along curves that map to parallel circles under the same isometry.*

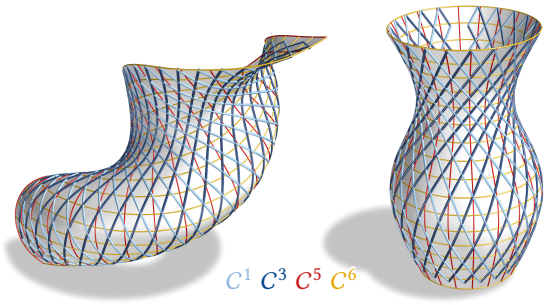

Fig. 9. On the *left*: A surface isometric to the surface of revolution shown on the *right*. A geodesic alignable net C^1, C^3 runs symmetrically to curves C^5, C^6 which map respectively to meridians and parallels under the isometry. Additionally, the angle that curves C^1 and C^3 make with curves C^5 is constant along curves C^6.

Proof. Assume that $\{C^1, C^3\}$ is a geodesic alignable net. We now show that the net must lie on a surface isometric to a surface of revolution. Let us consider the double frame of the net as described in Section 2.5. For a geodesic net, we have $g_1 = 0$ and $g_3 = 0$. Proposition 6 implies then $\mathbf{d}\alpha(\mathbf{e}_1) = \mathbf{d}\alpha(\mathbf{e}_3)$. For Proposition 4, we observe that the angle α is constant along the bisecting direction $\mathbf{e}_3 - \mathbf{e}_1$, and therefore that the 1-form $\mathbf{d}\alpha$ points along the bisecting direction $\mathbf{e}_1 + \mathbf{e}_3$.

Consider now a bisecting net $\{C^5, C^6\}$, with unit tangent vectors $\mathbf{e}_5 = (\mathbf{e}_1 + \mathbf{e}_3)/\|\mathbf{e}_1 + \mathbf{e}_3\|$ and $\mathbf{e}_6 = (\mathbf{e}_3 - \mathbf{e}_1)/\|\mathbf{e}_3 - \mathbf{e}_1\|$. Then consider the orthonormal basis $\{\mathbf{e}_5, \mathbf{e}_6\}$, and the dual-basis $\{\boldsymbol{\theta}^5, \boldsymbol{\theta}^6\}$. Let $\beta = \alpha/2$ be the angle that the vector $\mathbf{e}_1$ makes with the vector $\mathbf{e}_5$. Note that the angle α, as well as β, are constant in direction $\mathbf{e}_6$. Since $2\mathbf{d}\beta = \mathbf{d}\alpha$, we also have $\mathbf{d}\beta(\mathbf{e}_1) = \mathbf{d}\beta(\mathbf{e}_3)$. We can now write:

$$\mathbf{e}_1 = \mathbf{e}_5 \cos\beta - \mathbf{e}_6 \sin\beta, \quad \text{and} \quad \mathbf{e}_3 = \mathbf{e}_5 \cos\beta + \mathbf{e}_6 \sin\beta. \tag{3.8}$$

Let then $\boldsymbol{\omega}_{56}$ be the first connection form of Equations 2.12. From Equations 2.21, we get:

$$\begin{aligned} g_1 &= g_5 \cos\beta - g_6 \sin\beta - \mathbf{d}\beta(\mathbf{e}_1) = 0, \\ g_3 &= g_5 \cos\beta + g_6 \sin\beta + \mathbf{d}\beta(\mathbf{e}_3) = 0. \end{aligned} \tag{3.9}$$

Since $\mathbf{d}\beta(\mathbf{e}_1) = \mathbf{d}\beta(\mathbf{e}_3)$, summing Equations 3.9 yields $g_5 \cos\beta = 0$. For non degenerate curve nets, this implies $g_5 = 0$. The first structure Equation 2.13 implies then $\mathbf{d}\boldsymbol{\theta}^5 = 0$. Now, Equations 3.9 tell us $\mathbf{d}\beta(\mathbf{e}_1) = \mathbf{d}\beta(\mathbf{e}_3) = -g_6 \sin\beta$. Propositions 2 and 4 imply then $\mathbf{d}\beta \wedge \boldsymbol{\theta}^5 = 0$, and therefore $\mathbf{d}\beta(\mathbf{e}_6) = 0$. Together with Equations 3.8, we observe that $\mathbf{d}\beta(\mathbf{e}_5) = \sec\beta\, \mathbf{d}\beta(\mathbf{e}_1)$, and thus:

$$\mathbf{d}\beta = -g_6 \tan\beta\, \boldsymbol{\theta}^5. \tag{3.10}$$

Since $\mathbf{d}\boldsymbol{\theta}^5 = 0$, Proposition 3 tells us that $g_6 \tan\beta$ is constant in direction $\mathbf{e}_6$. As β is constant in direction $\mathbf{e}_6$, we conclude that g_6 is also constant in the direction $\mathbf{e}_6$. Summarizing, the curves C^5 are geodesics, and the orthogonal curves C^6 have constant geodesic curvature. According to Proposition 9 (in Appendix B), the surface is therefore isometric to a surface of revolution.

To prove that all surfaces isometric to a surface of revolution admit a geodesic alignable net, consider now a surface of revolution and trace on it a geodesic curve C. Construct curves C^1, C^3 by rotating around the axis, respectively, the curve C and its reflection about a meridian plane. By rotational symmetry, we have $g_1 = 0$, $g_3 = 0$, and $\mathbf{d}\alpha(\mathbf{e}_1) = \mathbf{d}\alpha(\mathbf{e}_3)$, which imply alignability for Proposition 6. All these quantities are preserved by isometry. □

We can easily observe that the equivalent condition for Chebyshev nets is much more restrictive. Indeed:

Corollary 1. *A geodesic Chebyshev net exists only and on all developable surfaces.*

Proof. Plugging Equations 3.7 into Equations 3.9, we get $g_5 = 0$ and $g_6 = 0$. We have then $\boldsymbol{\omega}_{56} = 0$ and therefore $\mathbf{d}\boldsymbol{\omega}_{56} = 0$. Cartan's structural equation 2.15 implies $K = 0$. □

3.4 Normal curvature-preserving alignable nets

We examine now alignable nets in which, at every point, the normal curvatures of curves C^1 and C^3 are equal, and where these normal curvatures vary at the same rate along the two curves. In this scenario, the net allows the extraction of a gridshell formed by congruent planar lamellae, shaping the curve in which it collapses, arranged orthogonally to the net surface $\mathcal{S}$. Consequently, we define a normal curvature-preserving alignable net as follows:

Definition 6. *Let $\{C^1, C^3\}$ be an alignable net on a surface $\mathcal{S}$, with normal curvatures n_1 and n_3. The net is normal curvature-preserving if, at each point of $\mathcal{S}$, $n_1 = n_3$ and $\mathbf{d}n_1(\mathbf{e}_1) = \mathbf{d}n_3(\mathbf{e}_3)$.*

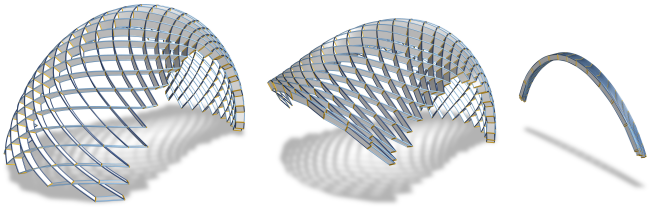

Fig. 10. A constant normal curvature alignable gridshells. The structure collapses onto a circular strip.

Also in this case, this additional condition imposes a constraint on the shape of the surface $\mathcal{S}$. Specifically:

Theorem 2. *A normal curvature-preserving alignable net exists only and on all surfaces that, at each point, satisfy the relation*

$$aK + bH + c = 0, \quad \text{with} \quad b^2 - 4ac <= 0, \tag{3.11}$$

where the coefficients a, b, and c are constant along one family of principal curvature lines, and where K and H are respectively the Gaussian and the mean curvature of the net surface. At each point, the normal curvature of the net is given by

$$n = \frac{-b}{2a}.$$

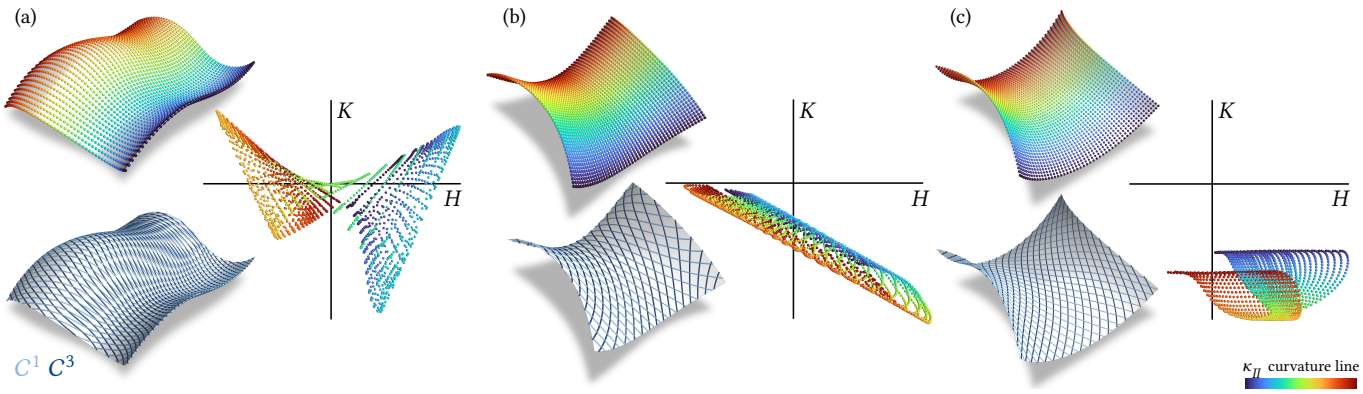

Fig. 11. (a) A tensor product B-spline approximating a PHLW-surface. *Top left*: Surface points belonging to the same curvature line corresponding to κ_{II} are visualized with the same color. *Right*: Each surface point is represented in a plane where coordinates are given by its mean curvature H and its Gaussian curvature K. This representation is termed *curvature diagram*. The alignment of points of the same color along a straight line indicates a linear correlation $aK + bH + c = 0$ along principal curvature lines. *Bottom left*: Curves C^1, C^3 with normal curvature $-b/2a$ form an alignable net which preserves normal curvature during the alignment. (b) A similar representation of a tensor product B-spline approximating a PHLW-surface with constant normal curvature. In the curvature diagram, point of the same color align along parallel lines. (c) A tensor product B-spline approximating a PK-surface. In the curvature diagram, points of the same color align along horizontal lines, indicating a constant Gaussian curvature. *Bottom left*: The asymptotic net C^1, C^3 of this surface is alignable.

Proof. Consider the double frame of the net depicted in Section 2.5. From the first Mainardi-Codazzi equation 2.16, written for both frames $\{\mathbf{e}_1, \mathbf{e}_2\}$ and $\{\mathbf{e}_3, \mathbf{e}_4\}$, we obtain respectively:

$$\begin{aligned} \mathbf{d}t_1(\mathbf{e}_1) - \mathbf{d}n_1(\mathbf{e}_2) &= g_1(n_2 - n_1) - 2g_2t_1, \\ \mathbf{d}t_3(\mathbf{e}_3) - \mathbf{d}n_3(\mathbf{e}_4) &= g_3(n_4 - n_3) - 2g_4t_3. \end{aligned} \tag{3.12}$$

Euler's equations 2.9 reveal that the condition $n_1 = n_2$ of Definition 6 is equivalent to the condition that the directions $\mathbf{e}_1$ and $\mathbf{e}_3$ are symmetric to principal curvature directions. Moreover, we observe that for such a principal symmetric net, we have $n_2 = n_4$ and $t_1 = -t_3$. From Equations 2.21, we can write:

$$\begin{aligned} g_2 &= g_3 \csc\alpha - g_1 \cot\alpha - \mathbf{d}\alpha(\mathbf{e}_3) \csc\alpha, \\ g_4 &= g_3 \cot\alpha - g_1 \csc\alpha - \mathbf{d}\alpha(\mathbf{e}_1) \csc\alpha. \end{aligned} \tag{3.13}$$

Let then $\beta = \alpha/2$ be the angle that directions $\mathbf{e}_1$ and $\mathbf{e}_3$ make with the principal curvature direction relative to κ_I. From Equations 3.12, expressing n_2 and t_1 as functions of the angle β with Euler's equations 2.9, substituting $n_2 = n_4$ and $t_1 = -t_3$, and plugging Equations 3.13, we get:

$$\begin{aligned} \mathbf{d}t_1(\mathbf{e}_1) - \mathbf{d}n_1(\mathbf{e}_2) &= (\kappa_{II} - \kappa_I)(g_3 - \mathbf{d}\alpha(\mathbf{e}_3)), \\ -\mathbf{d}t_1(\mathbf{e}_3) - \mathbf{d}n_1(\mathbf{e}_4) &= (\kappa_{II} - \kappa_I)(g_1 + \mathbf{d}\alpha(\mathbf{e}_1)). \end{aligned} \tag{3.14}$$

A detailed derivation is provided in Appendix B.

For points where $\kappa_I = \kappa_{II}$ (umbilical points), Euler's equations 2.9 imply $n_1 = n_3$ for all net directions. In all-umbilical regions, which are necessarily parts of planes or spheres (see [O'Neill 2006] p. 276), we further have $\mathbf{d}n_1 = \mathbf{d}n_3 = 0$. From Definition 6, we observe that all alignable nets are normal curvature-preserving.

For points where $\kappa_I \neq \kappa_{II}$, according to Proposition 6, the net is alignable if and only if $g_1 + \mathbf{d}\alpha(\mathbf{e}_1) = -g_3 + \mathbf{d}\alpha(\mathbf{e}_3)$ and therefore if and only if

$$\mathbf{d}t_1(\mathbf{e}_1) - \mathbf{d}n_1(\mathbf{e}_2) = \mathbf{d}t_1(\mathbf{e}_3) + \mathbf{d}n_1(\mathbf{e}_4). \tag{3.15}$$

Consider now the condition $\mathbf{d}n_1(\mathbf{e}_1) = \mathbf{d}n_1(\mathbf{e}_3)$ of Definition 4. Since the vectors $\mathbf{e}_1 - \mathbf{e}_3$ and $\mathbf{e}_2 + \mathbf{e}_4$ are parallel, from Proposition 4 we deduce $-\mathbf{d}n_1(\mathbf{e}_2) = \mathbf{d}n_1(\mathbf{e}_4)$. From Equation 3.15 we deduce then $\mathbf{d}t_1(\mathbf{e}_1) = \mathbf{d}t_1(\mathbf{e}_3)$. Therefore, for Proposition 4, we observe that along the principal curvature direction $\mathbf{e}_3 - \mathbf{e}_1$ the normal curvature n_1 and the geodesic torsion t_1 are both constant. From Euler's equations 2.9, employing the equations for the bisecting angle of sine and cosine with $\alpha = 2\beta$, we can derive the following relations, valid for all surfaces:

$$n = H + r\cos\alpha, \quad t = r\sin\alpha, \quad \text{with} \quad r = \sqrt{H^2 - K}.$$

Now, observing that $(n - H)^2 + t^2 = r^2$, we get:

$$K - 2n_1H + n_1^2 + t_1^2 = 0. \tag{3.16}$$

Multiplying by a the relation 3.16, and setting $b = -2an_1$ and $c = a(n_1^2 + t_1^2)$, yields the result. Moreover, we have $b^2 - 4ac = -4a^2t_1^2$, which is non-positive. □

We note that surfaces satisfying the conditions of Theorem 2 encompass linear Weingarten surfaces of hyperbolic type, which are surfaces where the coefficients of Equation 3.11 are constant at all points. Therefore, we propose the term *principal linear Weingarten surfaces of hyperbolic type*, abbreviated as *PHLW-surfaces*, to denote the broader class of surfaces defined by Theorem 2 (see Figure 11a).

If the normal curvature n of the net remains constant across all points on the surface, it becomes possible to extract an alignable gridshell that collapses into a planar circular arc (see Figures 10 and 11b). In this case:

Corollary 2. *An alignable gridshell with constant normal curvature n exists only and on all surfaces where the function $K - 2nH + n^2$ is constant and non-positive along one family of principal curvature lines.*

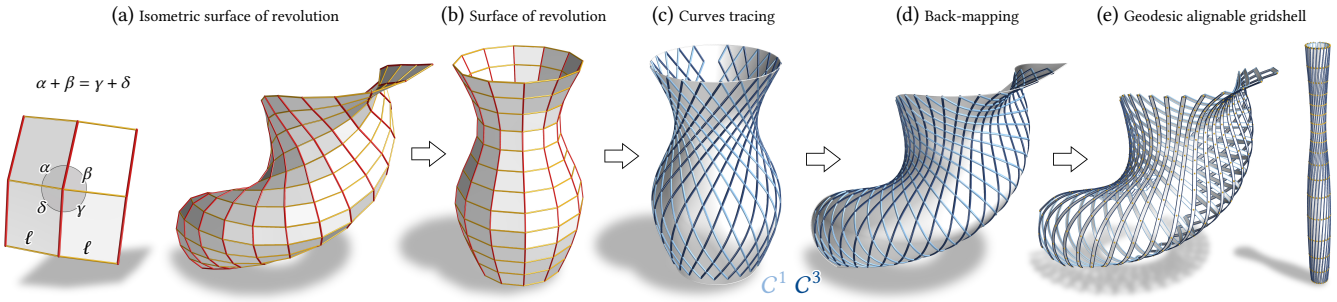

Fig. 12. Design of geodesic alignable gridshells. (a) We employ a geodesic parallel mesh discretization to design a surface isometric to a surface of revolution ([Wang et al. 2019]). This mesh is achieved when, at every vertex, the two sums of edge angles across each polyline of one family (*red*) are equal. The mesh becomes isometric to a surface of revolution if the polylines in the other family (*yellow*) have equal edge lengths along their paths. (b) We reconstruct an isometric surface of revolution, (c) and trace the alignable net on this surface by rotating and reflecting a single geodesic curve. (d) This net is then mapped back onto the initially designed surface. (e) The resulting curves can be used as the axes of a geodesic alignable gridshell.

Proof. We have $\mathbf{d}n = 0$. The proof follows directly from Theorem 2. □

A special case of alignable gridshells with preserving normal curvature are asympthotic alignable gridshells. In this case, beams can be realized with straight lamellae arranged orthogonally to the surface. In this scenario, the shape of the surface is constrained as follows:

Corollary 3. *An asymptotic alignable gridshell exists only and on all surfaces where the Gaussian curvature is constant and non-positive along one family of principal curvature lines.*

Proof. Given $n = 0$, the proof follows immediately from Theorem 2. □

In this case, we note that surfaces possessing the property outlined in Corollary 3 encompass surfaces with constant negative Gaussian curvature, also called K-surfaces. This expanded category is denoted as *PK-surfaces*, with the letter P signifying principal (see Figure 11c).

Equivalent conditions for normal curvature-preserving Chebyshev nets, previously outlined in [Liu et al. 2023], are provided in Appendix C.

4 COMPUTATIONAL DESIGN OF ALIGNABLE LAMELLA GRIDSHELLS

We now leverage our finding and propose two computational methods for the design of geodesic and normal curvature-preserving alignable nets. Both pipelines start with a first surface design step, followed by a curves tracing procedure. A lamella gridshell is then constructed using these curves as central axes of beams.

4.1 Design of geodesic alignable gridshells

This section outlines a computational pipeline for designing geodesic alignable nets. Following Theorem 1, the pipeline starts with the design of a surface which is isometric to a surface of revolution. Subsequently, the corresponding surface of revolution is reconstructed, and geodesic curves are traced on this surface. Finally, these curves are mapped back onto the isometric surface initially designed to get a geodesic alignable gridshell.

4.1.1 Surface design. To design a surface isometric to a surface of revolution, we employ the method introduced by Wang et al. [2019]. This approach relies on a regular quadrilateral mesh where the two families of edge polylines discretize a geodesic parallel parametrization of a surface — that is, an orthogonal parametrization where one family of parameter curves are geodesics. This property is ensured by enforcing, at each vertex, the constraint that sums of edge angles opposite to one family of polylines are equal (see Figure 12a). Isometry with a surface of revolution is achieved if each polyline within the other family possesses uniform edge lengths along its path. Within this discrete model, on such a mesh the two families of edge polylines will map respectively to meridians and parallels of a surface of revolution under an isometric deformation. This constrained mesh can approximate a given target surface, or be used for interactive modeling. For further details about this method and its implementation, we refer to [Wang et al. 2019].

4.1.2 Curves tracing. From the rotational isometric mesh, it is possible to derive the corresponding discrete surface of revolution using straightforward geometric considerations, as detailed in [Wang et al. 2019]. Once this surface is obtained, we proceed to lay out the alignable net upon it. According to Theorem 1, this net exhibits symmetry along meridians, and constant angle along parallel circles. Therefore, the net is uniquely defined by tracing a single geodesic curve from either C^1 or C^3. To trace this curve, it is possible to leverage Clairaut's relation, which states that any geodesic on a surface of revolution fulfills, at each point, $r \cos \xi = c$, where r is the distance of the geodesic to the axis of revolution, ξ measures the angle between the geodesic and the parallel circle passing through that point, and c is a constant. The curve can be constructed through a forward integration procedure, starting from a boundary parallel circle. All different geodesic curves can be obtained by varying the constant c. To achieve a smoother net, it is possible to interpolate the discrete rotational mesh with a NURBS surface.

The first family of curves can be obtained by rotating the traced curve around the axis of revolution. By first reflecting the traced curve about a meridian plane, we can obtain the second family of curves with the same procedure. To design a gridshell, the spacing

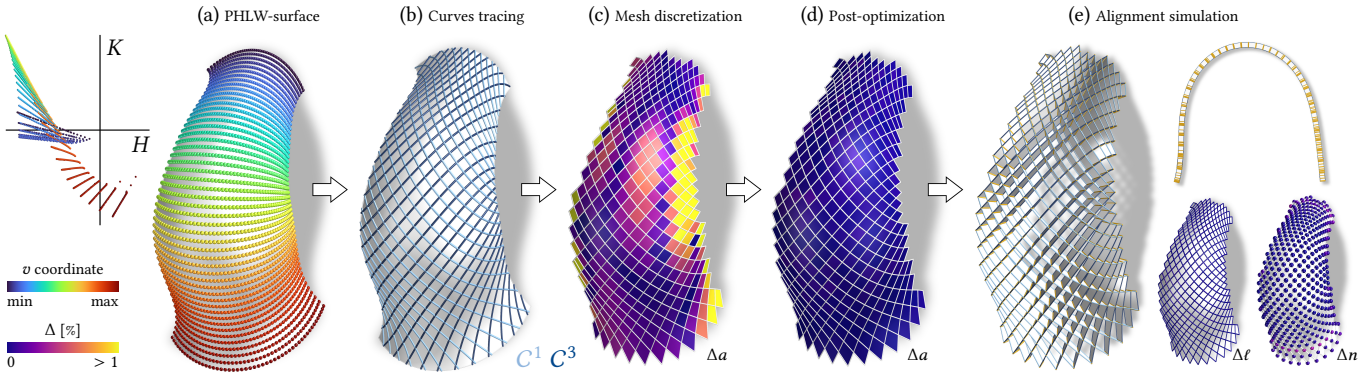

Fig. 13. Design of normal curvature-preserving alignable gridshells. (a) A PHLW-surface designed using our method (see Section 4.2.1), alongside its curvature diagram in the H-K plane. The u and v iso-parameter lines coincide with principal curvature lines. Points sharing the same u coordinate are depicted in the same color. (b) We trace the alignable net, which runs symmetrically to principal curvature directions (see Section 4.2.2). (c) To assess the alignability of the net, we employ a quad mesh discretization. The alignability error Δa is calculated for each face as the difference between the sums of opposing pairs of edge lengths, divided by the mean edge length. (d) We optimize the mesh to reduce alignability errors (see Section 4.2.4). (e) To simulate alignment, the mesh is collapsed onto a plane. Alignment is now achieved with minimal variations in edge lengths $\Delta\ell$ and discrete normal curvatures Δn.

between every curve can be varied as desired (see Figure 18). However, for architectural applications, it is often desirable to maintain uniform spacing in both families. This can be achieved by rotating the curve at equal intervals. Finally, the resulting net is mapped back onto the isometric surface to obtain the final gridshell. This procedure is summarized in Figure 12.

4.2 Design of normal curvature-preserving alignable gridshells

This section outlines a computational pipeline for designing normal curvature-preserving alignable nets. Leveraging Theorem 2, the pipeline starts with the design of a PHLW-surface. Subsequently, the alignable net is traced on this surface, and the collapsing curve of the net is reconstructed. Finally, we introduce a post-optimization procedure to mitigate potential errors, based on a mesh discretization of the curve net, and a deployment simulation that exploits geometric constraints within this mesh.

4.2.1 Surface design. To design a PHLW-surface, we optimize an input B-spline surface towards a PHLW curvature relation. For that, we build upon a method proposed in [Pellis et al. 2021] for the design of Weingarten surfaces.

As in [Pellis et al. 2021], the surface $\mathcal{S}$ is represented as a tensor product B-spline

$$S(u,v) = \sum_i \sum_j N_i^{d_u}(u) N_j^{d_v}(v)\, C_{ij}, \tag{4.1}$$

where C_{ij} are the control points, forming a quadrilateral mesh, while N_i^d denotes the B-spline basis functions of degree d. The degrees in the u and v directions are denoted as d_u and d_v respectively.

In this method, all constraints and target functions must be expressed as quadratic functions of variables. The primary variables of this problem are the positions of the control points C_{ij}. The target function is evaluated at sample points $\dot{S} = S(\dot{u}, \dot{v})$. The samplings $\dot{u}$ and $\dot{v}$ are determined through homogeneous subdivision of the u and v domains. Users have the flexibility to specify the bi-degree (d_u, d_v) of the B-spline surface, and they can control the density of the samples.

To express the PHLW condition of equation 3.11 as a quadratic constraint, the following auxiliary variables and corresponding constraints are introduced at each sample point $\dot{S}$: The non-unitized surface normal $\mathbf{u}$, with constraint

$$\mathbf{u} = S_{,u} \times S_{,v}. \tag{4.2}$$

The coefficients of the first fundamental form E, F and G, with constraints

$$E = \langle S_{,u}, S_{,u} \rangle, \quad F = \langle S_{,u}, S_{,v} \rangle, \quad G = \langle S_{,v}, S_{,v} \rangle, \tag{4.3}$$

where angle brackets indicate the dot product between two vectors. The determinant of the first fundamental form δ, with constraint

$$\delta = EG - F^2. \tag{4.4}$$

The coefficients of the second fundamental form L, M and N, with constraints

$$L = \frac{\langle S_{,uu}, \mathbf{u} \rangle}{\sqrt{\delta}}, \quad M = \frac{\langle S_{,uv}, \mathbf{u} \rangle}{\sqrt{\delta}}, \quad N = \frac{\langle S_{,vv}, \mathbf{u} \rangle}{\sqrt{\delta}}. \tag{4.5}$$

The Gaussian curvature K and the mean curvature H, defined by constraints

$$K = \frac{LN - M^2}{\delta}, \quad H = \frac{LG - 2MF - NE}{2\delta}. \tag{4.6}$$

Here, the surface derivatives $S_{,u}$, $S_{,v}$, $S_{,uu}$, $S_{,uv}$, and $S_{,vv}$ can be derived analytically from the B-spline equation 4.1, and exhibit a linear dependency on the control points C_{ij} (see [Prautzsch et al. 2002]). More details on this implementation can be found in [Pellis et al. 2021].

To enforce the linear relation of Equation 3.11 along principal curvature lines, we employ a principal curvature parametrization for the u and v coordinates of the B-spline surface. This is achieved by introducing constraints

$$F = 0, \quad M = 0, \tag{4.7}$$

at each sample point $S(\dot{u}, \dot{v})$. Then, we define the target function of Equation 3.11 as

$$K - 2n_{\dot{u}}H + n_{\dot{u}}^2 + t_{\dot{u}}^2 = 0, \tag{4.8}$$

where $n_{\dot{u}}$ and $t_{\dot{u}}$ are two additional variables defined for each sampled coordinate $\dot{u}$. To create alignable nets with constant normal curvature, we set $n_{\dot{u}}$ as a unique variable for all points. For asymptotic alignable nets, we impose $n_{\dot{u}} = 0$. Denoting the residual of i-th constraint of Equations 4.2 to 4.7 as χ_i, and the residual of the target function 4.8 as χ_t, we define a PHLW energy as:

$$E_{\text{PHLW}} = \sum_{\dot{S}} \left(\sum_i \chi_i^2 + \omega_t \chi_t^2 \right),$$

where ω_t denotes a weight, which we set to 10^{-1}.

To prevent the formation of a degenerate net — where the angle β that directions $\mathbf{e}_1$ and $\mathbf{e}_3$ make with a principal curvature direction is 0 or $\pm\pi/2$ — from Euler's equations 2.9 we observe that, at a sample point $\dot{S}$, the angle β equals $\pi/4$ when $n_{\dot{u}} = H$. We introduce then a fairness energy E_β defined as:

$$E_\beta = \omega_\beta \sum_{\dot{S}} (n_{\dot{u}} - H)^2,$$

where ω_β was set to $5 \cdot 10^{-4}$.

To approximate a given reference surface S^r, we introduce a closeness energy E_c and a gliding energy E_g defined as follows:

$$E_c = \omega_c \sum_{\dot{S}} \|\dot{S} - S_c^r\|^2, \quad E_g = \omega_g \sum_{\dot{S}} \langle \dot{S} - S_c^r, \mathbf{u}_c^r \rangle^2,$$

where S_c^r is the closest point to $\dot{S}$ on the reference surface S^r, and $\mathbf{u}_c^r$ denotes the normal vector of S^r at P_c^r.

We solve then the optimization problem

$$E_{\text{PHLW}} + E_\beta + E_c + E_g \rightarrow \min.$$

This optimization is carried out using a Levenberg-Marquardt algorithm, implemented with the method proposed in [Tang et al. 2014]. During optimization, the variables $n_{\dot{u}}$ and $t_{\dot{u}}$ are initialized via linear fitting of the target function in Equation 4.8 to sample points with the same $\dot{u}$ coordinate. In all the examples presented, we used B-spline surfaces of bi-degree 4, with a grid of 9x9 control points, and a grid of 18x18 sample points.

4.2.2 Curves tracing. Once a B-spline surface S has been optimized towards a PHLW-surface, we can compute the unit tangent vectors of a principal curvature net $\{C^5, C^6\}$ at each sample point $S(\dot{u}, \dot{v})$ as follows:

$$\mathbf{e}_5 = \frac{S_{,u}}{\|S_{,u}\|}, \quad \mathbf{e}_6 = \frac{S_{,v}}{\|S_{,v}\|}.$$

The corresponding dual-basis is given by:

$$\boldsymbol{\theta}_5 = \|S_{,u}\| \, \mathbf{d}u, \quad \boldsymbol{\theta}_6 = \|S_{,v}\| \, \mathbf{d}v. \tag{4.9}$$

Next, we aim to compute the directions of the normal curvature-preserving alignable net, $\mathbf{e}_1$ and $\mathbf{e}_3$, forming an angle $\pm\beta$ with the principal curvature direction $\mathbf{e}_5$. At each sample point $S(\dot{u}, \dot{v})$, Euler's equations 2.9 yield:

$$\kappa_I \cos^2 \beta + \kappa_{II} \sin^2 \beta = n_{\dot{u}},$$

and consequently,

$$\sin^2 \beta = \frac{n_{\dot{u}} - \kappa_I}{\kappa_{II} - \kappa_I}. \tag{4.10}$$

The density of sampling $(\dot{u}, \dot{v})$ can be chosen independently of the one used in the preceding surface optimization (see Figure 14). For sample points sharing the same $\dot{u}$ coordinate, the normal curvature $n_{\dot{u}}$ can be determined through linear fitting using Equation 4.8. Subsequently, at each sample point, the net directions are computed as follows:

$$\mathbf{e}_1 = \cos\beta \, \mathbf{e}_5 - \sin\beta \, \mathbf{e}_6, \quad \mathbf{e}_3 = \cos\beta \, \mathbf{e}_5 + \sin\beta \, \mathbf{e}_6. \tag{4.11}$$

To trace a family of smooth curves on the surface $S(u, v)$, we exploit level-sets of a smooth surface function $\xi(u, v)$. The differential of the function ξ is given by:

$$\mathbf{d}\xi = \xi_{,u} \mathbf{d}u + \xi_{,v} \mathbf{d}v.$$

The level-sets of ξ align with the direction $\mathbf{e}_1$ when $\mathbf{d}\xi(\mathbf{e}_1) = 0$. Substituting $\mathbf{d}u$ and $\mathbf{d}v$ with Equations 4.9, and plugging $\mathbf{e}_1$ from Equations 4.11, we get:

$$\mathbf{d}\xi(\mathbf{e}_1) = \xi_{,u} \frac{\cos\beta}{\|S_{,u}\|} - \xi_{,v} \frac{\sin\beta}{\|S_{,v}\|} = 0. \tag{4.12}$$

Consider now the direction $\mathbf{e}_2 = \sin\beta \, \mathbf{e}_5 + \cos\beta \, \mathbf{e}_6$, which is orthogonal to $\mathbf{e}_1$. The density of level-sets of ξ at each surface point is given by:

$$\mathbf{d}\xi(\mathbf{e}_2) = \xi_{,u} \frac{\sin\beta}{\|S_{,u}\|} + \xi_{,v} \frac{\cos\beta}{\|S_{,v}\|}. \tag{4.13}$$

The same applies for direction $\mathbf{e}_3$ and its orthogonal direction $\mathbf{e}_4$.

To compute the function ξ, we employ a B-spline surface $F(u, v)$, defined on the same u, v parameter space of the B-spline surface S, such that $F(u, v) = (u, v, \xi)^T$. The variables are then the ξ-coordinates of the control points of F. The number of control points in u and v directions can be set by the user. Alignment with the specified

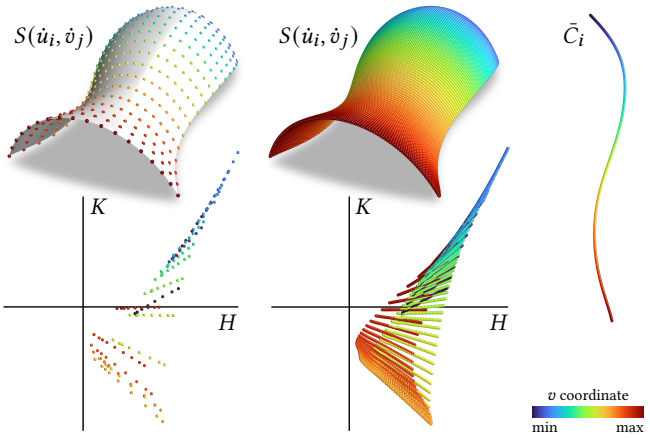

Fig. 14. On the *left*, sampling points employed for the optimization of the B-spline surface towards a PHLW relation, as described in Section 4.2.1. In the *center*, the PHLW relation persists even increasing the sampling density, indicating a smooth solution. On the *right*: Collapse polyline composed of points $\bar{C}_i$. To reconstruct the collapse curve, we maintain a uniform sample density of 1200x1200 across all presented results.

direction is enforced at sample points $\dot{F} = F(\dot{u}, \dot{v})$. In particular, we define an alignment energy E_a and a fairness energy E_f as follows:

$$E_a = \sum_{\dot{F}} \mathbf{d}\xi(\mathbf{e}_1)^2, \quad E_f = \omega_f \sum_{\dot{F}} (\mathbf{d}\xi(\mathbf{e}_2) - 1)^2,$$

where we use Equations 4.12 and 4.13 evaluated at each sample point $\dot{F}$, and set a fixed weight ω_f to 10^{-1}. Note that the partial derivatives $\xi_{,u}$ and $\xi_{,v}$ depend linearly on the control points. Then, we solve the energy minimization with a Levenberg-Marquardt method (refer to [Tang et al. 2014]). In the presented examples, we used B-splines F of bi-degree 3, with 12x12 control points, and 48x48 sample points. Curves C^1 and C^3 are then traced by connecting points with equal ξ values. These values are obtained through a uniform subdivision of the ξ domain, with the subdivision density adjustable by the user.

4.2.3 Collapse curve reconstruction. We aim now to reconstruct the collapse curve of the net. We begin by densely sampling the PHLW-surface $S(u, v)$ with $(\dot{u}, \dot{v})$ pairs. Then, we leverage the property that for each fixed parameter value $\dot{u}_i$ all corresponding surface points $S(\dot{u}_i)$ are expected to collapse onto a single point, denoted as $\bar{C}_i$, on the collapse curve (see Figure 14). Next, we construct a collapse polyline connecting points $\bar{C}_i$, and discretize the arc-length between a point $\bar{C}_i$ and its consecutive point $\bar{C}_{i+1}$ as chord-length $\|\bar{C}_i - \bar{C}_{i+1}\|$, computed as follows:

$$\|\bar{C}_i - \bar{C}_{i+1}\| = \frac{1}{m} \sum_{j=1}^{m} \frac{\|S(\dot{u}_i, \dot{v}_j) - S(\dot{u}_{i+1}, \dot{v}_j)\|}{\cos \beta(\dot{u}_i, \dot{v}_j)}, \tag{4.14}$$

where m is the number of $\dot{v}$ samples and $\beta(\dot{u}_i, \dot{v}_j)$ is the angle that the net makes with the first principal curvature direction at sample point $S(\dot{u}_i, \dot{v}_j)$, given by Equation 4.10. Here, for each sample $\dot{u}_i$, we computed an average between sample points $S(\dot{u}_i, \dot{v}_j)$ to account for potential discrepancies arising from discretization and PHLW-surface optimization.

Now, we observe that the normal curvature of the net at surface points $S(\dot{u}_i)$ is constant. We acquire this curvature, denoted as n_i, through linear fitting at sample points $S(\dot{u}_i, \dot{v}_j)$ using Equation 4.8. The normal curvature n_i shall equal the curvature of the collapse curve at the point $\bar{C}_i$, which we discretize as the inverse radius of the circle passing through points $\bar{C}_i$, $\bar{C}_{i-1}$, and $\bar{C}_{i+1}$. Points $\bar{C}_i$, along with the flattened surface normal $\bar{\mathbf{n}}_i$, are then derived through a forward integration at sample coordinates $\dot{u}_i$, as detailed in Figure 15.

$$s = \operatorname{sign}(n_i)$$
$$\vartheta_i = \arcsin\left(|n_i| \frac{\ell_{i-1}}{2}\right)$$
$$\lambda_i = \arcsin\left(|n_i| \sqrt{\left(\frac{1}{n_i}\right)^2 - \left(\frac{\ell_i}{2}\right)^2}\right)$$
$$\gamma_i = \gamma_{i-1} - s\,(\lambda_i - \vartheta_i - \pi/2)$$
$$\bar{\mathbf{n}}_i = (\sin(\gamma_{i-1} - s\vartheta_i), -\cos(s\vartheta_i - \gamma_{i-1}))$$
$$\bar{C}_{i+1} = \bar{C}_i + \ell_i(\cos\gamma_i, \sin\gamma_i)$$

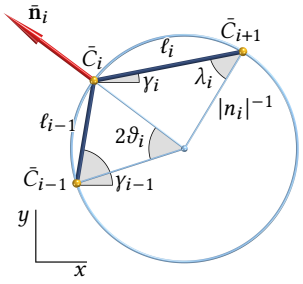

Fig. 15. Reconstruction of the collapse curve at i-th iteration. On the *right*: Configuration of aligned points $\bar{C}_i$, along with the parameters involved in forward integration. The lengths ℓ_i are computed with Equation 4.14.

4.2.4 Post-optimization and alignment simulation. To achieve the precision required for real-world manufacturing, we refine the curve net through a post-optimization process. For that, we employ a mesh discretization wherein adjacent curve joints are connected by straight edges. We denote the vertices of this mesh as V_j. We compute then the position of these vertices after alignment, denoted as $\bar{V}_j$. To do that, we extract the u coordinate of V_j on the surface, and map it onto the aligned polyline $\bar{C}_i$ through barycentric coordinates. Then, we simultaneously optimize the positions of vertices V_j and the aligned configuration $\bar{V}_j$ by modeling a deployment process of the mesh. In this process, edge lengths are preserved, and edges rotate at each vertex around a common axis.

In this optimization, the variables consist of the positions of vertices $V_j \in \mathbb{R}^3$, their corresponding rotation axes $\mathbf{r}_j \in \mathbb{R}^3$, the aligned positions $\bar{V}_j \in \mathbb{R}^2$, and the aligned rotation axes $\bar{\mathbf{r}}_j \in \mathbb{R}^2$. For each edge jk connecting vertices V_j and V_k, we ensure edge length preservation with the constraint

$$\chi_\ell = \|V_k - V_j\|^2 - \|\bar{V}_k - \bar{V}_j\|^2.$$

At each vertex V_j, we let edges jk to rotate around a common axis $\mathbf{r}_j$ by adding constraints

$$\chi_r = \langle V_k - V_j, \mathbf{r}_j \rangle - \langle \bar{V}_k - \bar{V}_j, \bar{\mathbf{r}}_j \rangle,$$

along with normalization constraints

$$\chi_u = \|\mathbf{r}_j\|^2 - 1, \quad \chi_{\bar{u}} = \|\bar{\mathbf{r}}_j\|^2 - 1.$$

Subsequently, the alignability energy E_a is formulated as:

$$E_a = \omega_\ell \sum_{jk} \chi_\ell^2 + \omega_r \sum_j \sum_k \chi_r^2 + \omega_u \sum_j (\chi_u^2 + \chi_{\bar{u}}^2).$$

To maintain proximity to the initial configuration of the mesh, we introduce point closeness and gliding energy terms

$$E_c = \omega_c \sum_j \|V_j - V_j^0\|^2, \quad E_g = \omega_g \sum_j \langle V_j - S_c, \mathbf{n}_c \rangle^2,$$

where V_j^0 represents the initial position of vertex V_j, while S_c and $\mathbf{n}_c$ respectively denote its closest point on the B-spline surface and the corresponding normal. Furthermore, we let the points $\bar{V}_j$ to glide on the collapsing curve $\bar{C}_i$ by introducing the energies

$$E_{\bar{c}} = \omega_{\bar{c}} \sum_j \|\bar{V}_j - \bar{C}_c\|^2, \quad E_{\bar{g}} = \omega_{\bar{g}} \sum_j \langle \bar{V}_j - \bar{C}_c, \bar{\mathbf{n}}_c \rangle^2,$$

where $\bar{C}_c$ and $\bar{\mathbf{n}}_c$ respectively denote the closest point $\bar{C}_i$ to $\bar{V}_j$, and the corresponding aligned normal $\bar{\mathbf{n}}_i$. To ensure consistency between rotation axes on the surface and the collapsing curve, we introduce the energies

$$E_s = \omega_s \sum_j \left(\langle \mathbf{r}_j, \mathbf{n}_c \rangle - 1\right)^2, \quad E_{\bar{s}} = \omega_{\bar{s}} \sum_j \left(\langle \bar{\mathbf{r}}_j, \bar{\mathbf{n}}_c \rangle - 1\right)^2.$$

Finally, to maintain mesh fairness, we introduce a graph Laplacian energy for vertices V_j, with a weight ω_f. We solve the minimization problem with a Levemberg-Marquardt algorithm (see [Tang et al. 2014]). Weights used for the presented examples are reported in Table 2.

For simulating the full deployment sequence of the net, we use a similar approach. The reference configuration is now the optimized mesh with vertices V_j^* and corresponding rotation axes $\mathbf{r}_j^*$, which

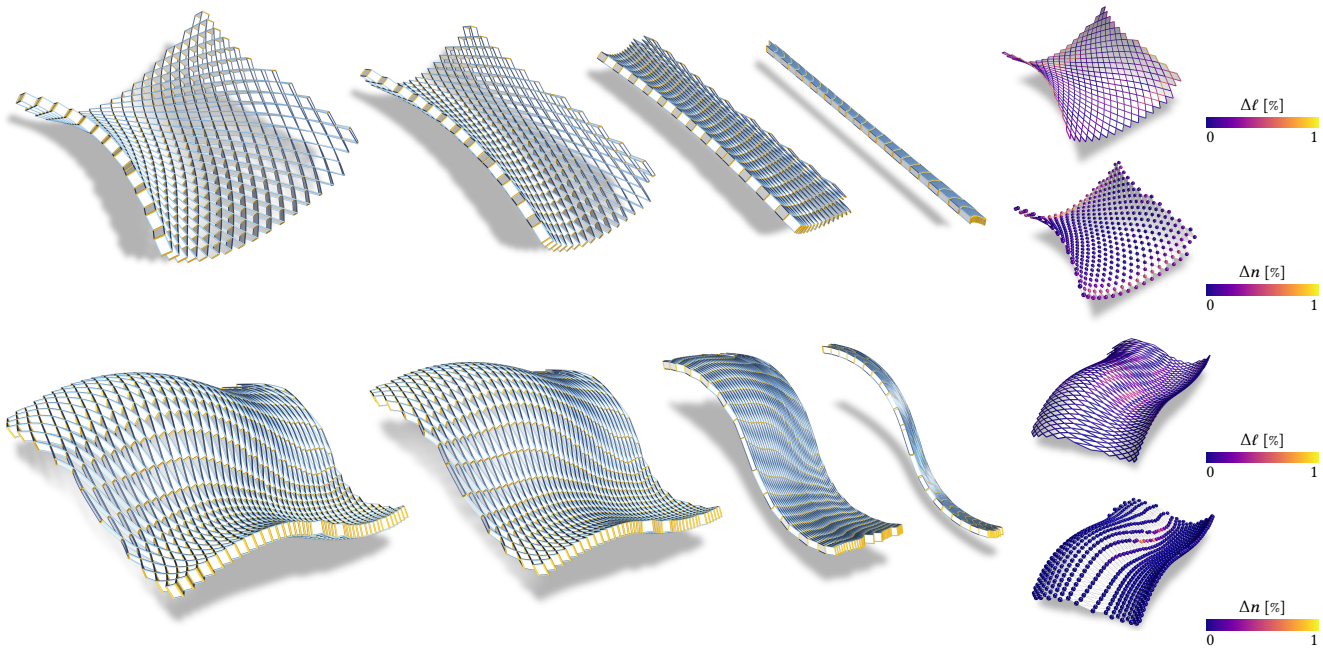

Fig. 16. Alignment sequence of normal curvature-preserving alignable gridshells. The gridshells are extracted from the PHLW-surfaces shown in Figure 11a and 11c, following a post-optimization. On the *right*, the variations in edge length $\Delta\ell$ and normal curvature Δn after complete alignment are shown.

are substituted for $\bar{V}_j$ and $\bar{\mathbf{r}}_j$ in the alignment energy E_a. The variables are the deployed vertices V_j and rotation axes $\mathbf{r}_j$. To collapse the mesh into a curve, we determine a collapse direction $\mathbf{d}$ by averaging the vectors between the first and last sample points of each $\dot{u}$ parameter line of the PHLW-surface. Then, we define energies to align vertices and vertex normals onto the plane with normal vector $\mathbf{d}$ and passing through the mesh centroid. Intermediate states can be achieved through affine combinations between weights of collapsing energies with the one of a proximity energy to V_j^*. In this case, we introduce a Laplacian fairness both for vertices V_j and rotation axes $\mathbf{r}_j$.

Table 2. Weights used for post-optimization of the presented results, as described in Section 4.2.4.

ω_ℓ	ω_r	ω_u	ω_c	ω_g	$\omega_{\bar{c}}$	$\omega_{\bar{g}}$	ω_s	$\omega_{\bar{s}}$	ω_f
1	10^2	10^2	$[10^{-5}, 10^{-4}]$	10^{-5}	10^{-1}	10^{-1}	10^{-2}	10^{-1}	$[10^{-5}, 10^{-4}]$

5 RESULTS AND DISCUSSION

In this section, we present and discuss the results obtained from the computational pipelines detailed in Section 4. All algorithms have been implemented using Python, alongside the numerical libraries NumPy and SciPy. The outcomes are shown in Figures 1, 4, 10 to 14, and 16 to 21. For implementation specifics and validation tests concerning the surface optimizations discussed in Sections 4.1.1 and 4.2.1, we refer to [Wang et al. 2019] and [Pellis et al. 2021], respectively. Further details about the Levemberg-Marquardt algorithm used in our implementation can be found in [Tang et al. 2014].

5.1 Verification of results

We assess the alignability of a curve net using a mesh discretization. On each face of this mesh, consider pairs of edge lengths (ℓ_1, ℓ_3) and (ℓ_2, ℓ_4) that will overlap upon alignment. An alignability error Δa is then calculated for each face as follows:

$$\Delta a = 4 \left| \frac{\ell_1 + \ell_2 - \ell_3 - \ell_4}{\ell_1 + \ell_2 + \ell_3 + \ell_4} \right|.$$

Our experiments consistently demonstrate low alignability errors Δa, with an average typically falling below 1%, and with a maximum remaining under 3% (as detailed in Figures 13 and 18). Furthermore, Figure 19 showcases that Δa exhibits a low dependence on mesh coarseness, decreasing consistently with mesh refinement.

For normal curvature-preserving networks, the post-optimization process outlined in Section 4.2.4 achieves a significant reduction in the error Δa by an order of magnitude, as visualized in Figure 13. Additionally, Figure 17 depicts the minimal deviation of the post-optimized mesh from the PHLW-surface, confirming the effectiveness of the inverse design pipeline.

To further assess the alignability of normal curvature-preserving nets, we performed simulations involving an alignment sequence where the mesh is collapsed onto a plane (as detailed in Section 4.2.4). We measure the relative differences in edge lengths $\Delta\ell$ and discrete normal curvature Δn between the optimized mesh and the aligned configuration using the following equations:

$$\Delta\ell = \left| \frac{|V_k^a - V_j^a| - |V_k^* - V_j^*|}{|V_k^* - V_j^*|} \right|,$$

$$\Delta n = \frac{1}{m} \sum_{k=1}^{m} \left| \frac{\langle V_j^a - V_k^a, \mathbf{r}_j^a \rangle - \langle V_j^* - V_k^*, \mathbf{r}_j^* \rangle}{\langle V_j^* - \bar{V}_k^*, \mathbf{r}_j^* \rangle} \right|,$$

where a and $*$ denote quantities in the aligned and post-optimized mesh, respectively, and k represents vertices connected to vertex j. Values found in our tests are shown in Figures 13 and 16. Notably, our experiments consistently yielded errors below 1%.

The pipeline for designing normal curvature-preserving alignable gridshells has been further validated through the construction of physical prototypes (refer to Figure 21). In this instance, post-optimization was executed on a denser mesh, with 16 faces per model face.

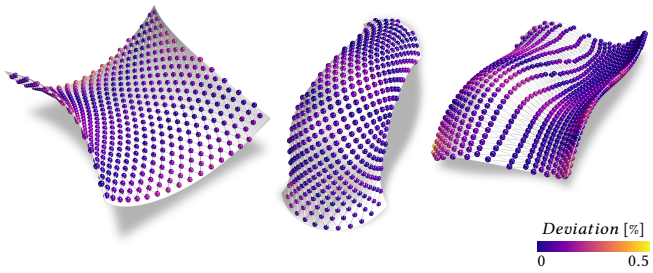

Fig. 17. Distance of mesh vertices from the original PHLW-surface, after post-optimization. Deviation is quantified as percentage of the bounding box diagonal of the PHLW-surface. We observe that post-optimization introduces minor deviations.

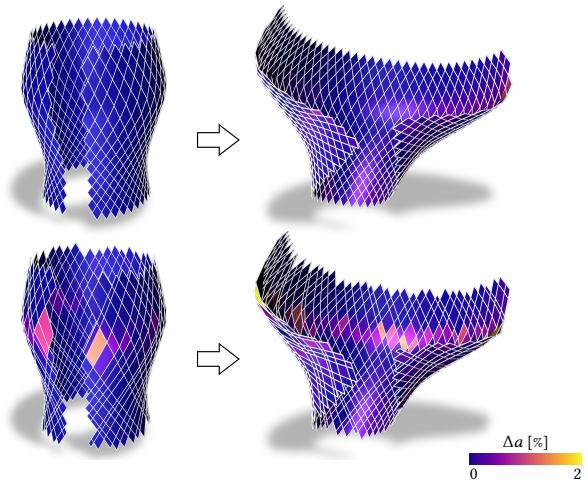

Fig. 18. Comparison of alignability errors Δa between a geodesic net on a surface of revolution and its isometric deformation. Minor error variations are induced by the isometric mapping of the net. *Top*: A net with uniform spacing. *Bottom*: Demonstrating alignability even with varying spacing between curves.

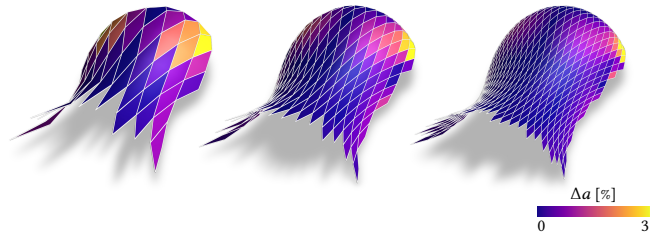

Fig. 19. Alignability error Δa of a normal curvature-preserving net across various mesh densities. We observe that the error remains consistent even for coarse discretizations.

5.2 Limitations

A fundamental constraint of the presented approach lies in the geometric simplification applied to the gridshell. Specifically, we assume that the beams exhibit no bending resistance along the wider cross-sectional direction, nor any torsional resistance. These assumptions are quite realistic when the cross-sections of the beams are inscribed in rectangles with an edge ratio of approximately 10:1 or higher. However, for beams with lower edge ratios, these neglected resistances can cause significant deviations in the final shape. To address this issue, one approach is to employ a simulation-based method as [Panetta et al. 2019] to refine the result. In this scenario, the presented pipelines serve as valuable initialization steps, enabling inverse design processes. Simulation-based methods can also be used to optimize the mechanical behavior of the structure by minimizing the elastic energy stored in the beams.

On the computational front, a notable limitation of the pipeline for normal curvature-preserving gridshells is encountered during the PHLW-surface optimization. Here, we are restricted to modeling surfaces with curvature lines forming a regular patch, devoid of singularities. In many cases, this entails a significant shape change of the input B-spline surface, making this method more suitable for interactive design rather than shape approximation (see Figure 20). Exploring methods capable of handling more complex shapes is left for future investigation.

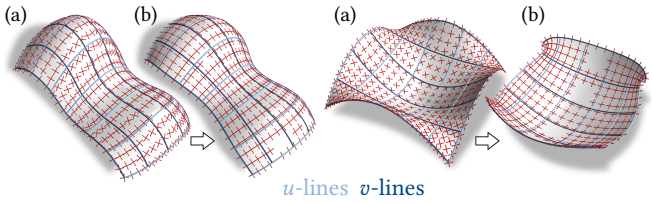

Fig. 20. Shape approximation with PHLW-surfaces. (a) Input B-spline. (b) Optimized B-spline, as detailed in Section 4.2.1. Principal curvature directions are indicated in *red*, where defined. On the *right*, an example of approximation failure is shown. The significant shape change is mainly due to the alignment of the u and v parameter curves with the principal curvature directions.

6 FINAL REMARKS

In this work, we addressed the design of deployable lamella gridshells by studying the geometric properties of alignable nets. First, it was shown that geodesic alignable nets exist only on surfaces isometric to a surface of revolution. This conclusion, originally highlighted by Tellier [2022a], follows intuitively from the rotational symmetry inherent in surfaces of revolution, coupled with the preservation of lengths and geodesic curvature during isometric transformations. However, this study revealed that such surfaces represent the sole configuration attainable for geodesic alignable nets. Furthermore, it was established that normal curvature-preserving alignable nets exist only on a special class of surfaces, named PHLW-surfaces, characterized by a consistent linear relation between curvatures along

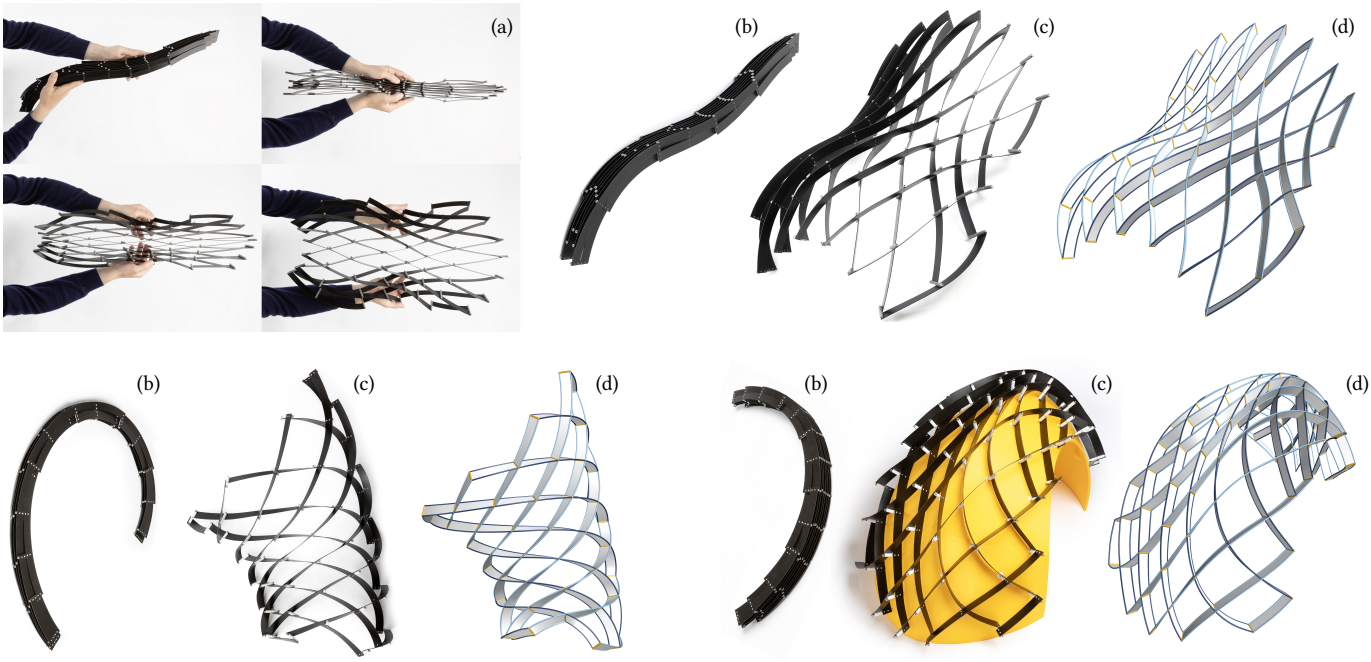

Fig. 21. Physical prototypes of normal curvature-preserving alignable gridshells, designed with the pipeline of Section 4.2. The lamellae, 20 mm wide each, are made by cutting 1 mm thick polypropylene sheets. (a) Deployment sequence. (b) Aligned configuration. (c) Deployed configuration. *Bottom right*, in *yellow*: The PHLW surface, offset by 20 mm, has been 3D printed and the joint locations have been marked. By placing the joints exactly in the expected locations, we observe a good shape match. (d) Digital model after post-optimization.

a family of principal curvature lines. In this case, unlike the equivalent Chebyshev nets which are limited to shaping rotational and cylindrical surfaces, the findings unveil a broader class of structures capable of collapsing into generic planar curves. Lastly, the author believes that these findings open avenues for exploring surfaces where even more complex curvature relationships, beyond simple linear ones, consistently hold along principal lines of curvature.

ACKNOWLEDGMENTS

The author is grateful to Alessandro Muntoni for the help with 3D printing, Andrea Favilli for the valuable mathematical discussions, and Nuri Rashid for the help with photographs.

This work has received financial support by the Horizon Europe Research & Innovation Programme under Grant agreement N. 101092612 (Social and hUman ceNtered XR - SUN project). Views and opinions expressed in this paper are those of the author only and do not necessarily reflect those of the European Union. Neither the European Union nor the European Commission can be held responsible for them.

REFERENCES

Quentin Becker, Seiichi Suzuki, Yingying Ren, Davide Pellis, Julian Panetta, and Mark Pauly. 2023. C-shells: Deployable Gridshells with Curved Beams. *ACM Trans. Graph.* 42, 6 (2023), 181:1–17.

Alexander I Bobenko and Yuri B Suris. 2008. *Discrete differential geometry: Integrable structure*. Vol. 98. American Mathematical Soc.

Pafnutij L. Chebyshev. 1878. Sur la coupe des vêtements. In *Association français pour l'avancement des science, Congres de Paris*. 154–155.

Tian Chen, Julian Panetta, Max Schnaubelt, and Mark Pauly. 2021. Bistable Auxetic Surface Structures. *ACM Trans. Graph.* 40, 4 (2021), 39:1–9.

Manfredo P. do Carmo. 1976. *Differential Geometry of Curves and Surfaces*. Prentice-Hall.

Lionel Du Peloux, Frédéric Tayeb, Jean-François Caron, and Olivier Baverel. 2015. The Ephemeral Cathedral of Créteil: a 350m2 lightweight gridshell structure made of 2 kilometers of GFRP tubes. In *CIGOS 2015:" Innovations in Construction"*.

Akash Garg, Andrew O Sageman-Furnas, Bailin Deng, Yonghao Yue, Eitan Grinspun, Mark Pauly, and Max Wardetzky. 2014. Wire mesh design. *ACM Trans. Graph.* 33, 4 (2014), 66:1–12.

Ruslan Guseinov, Eder Miguel, and Bernd Bickel. 2017. CurveUps: shaping objects from flat plates with tension-actuated curvature. *ACM Trans. Graph.* 36, 4 (2017), 64:1–12.

Christian Hafner and Bernd Bickel. 2021. The design space of plane elastic curves. *ACM Trans. Graph.* 40, 4 (2021), 126:1–20.

Yaoye Hong, Yinding Chi, Shuang Wu, Yanbin Li, Yong Zhu, and Jie Yin. 2022. Boundary curvature guided programmable shape-morphing kirigami sheets. *Nature Communications* 13, 1 (2022), 530:1–13.

Joe Kahlert, Matt Olson, and Hao Zhang. 2011. Width-bounded geodesic strips for surface tiling. *The Visual Computer* 27 (2011), 45–56.

Mina Konaković, Keenan Crane, Bailin Deng, Sofien Bouaziz, Daniel Piker, and Mark Pauly. 2016. Beyond developable: computational design and fabrication with auxetic materials. *ACM Trans. Graph.* 35, 4 (2016), 89:1–11.

Francesco Laccone, Luigi Malomo, Nico Pietroni, Paolo Cignoni, and Tim Schork. 2021. Integrated computational framework for the design and fabrication of bending-active structures made from flat sheet material. *Structures* 34 (2021), 979–994.

Daoming Liu, Davide Pellis, Yu-Chou Chiang, Florian Rist, Johannes Wallner, and Helmut Pottmann. 2023. Deployable Strip Structures. *ACM Trans. Graph.* 42, 4 (2023), 103:1–16.

Yannick Masson and Laurent Monasse. 2017. Existence of global Chebyshev nets on surfaces of absolute Gaussian curvature less than 2π. *Journal of Geometry* 108, 1 (2017), 25–32.

Saurabh Mhatre, Elisa Boatti, David Melancon, Ahmad Zareei, Maxime Dupont, Martin Bechthold, and Katia Bertoldi. 2021. Deployable Structures Based on Buckling of Curved Beams Upon a Rotational Input. *Advanced Functional Materials* 31, 35 (2021), 2101144:1–7.

Dragos Naicu, Richard Harris, and Chris Williams. 2014. Timber gridshells: Design methods and their application to a temporary pavilion. In *World Conference on Timber Engineering*. 10–14.
Tristan Needham. 2021. *Visual differential geometry and forms: A mathematical drama in five acts*. Princeton University Press.
Barrett O'Neill. 2006. *Elementary Differential Geometry*. Elsevier.
Julian Panetta, Florin Isvoranu, Tian Chen, Emmanuel Siéfert, Benoît Roman, and Mark Pauly. 2021. Computational inverse design of surface-based inflatables. *ACM Trans. Graph.* 40, 4 (2021), 40:1–14.
Julian Panetta, Mina Konaković-Luković, Florin Isvoranu, Etienne Bouleau, and Mark Pauly. 2019. X-shells: A new class of deployable beam structures. *ACM Trans. Graph.* 38, 4 (2019), 83:1–15.
Davide Pellis, Martin Kilian, Helmut Pottmann, and Mark Pauly. 2021. Computational Design of Weingarten Surfaces. *ACM Trans. Graph.* 40, 4 (2021), 114:1–11.
Davide Pellis, Hui Wang, Martin Kilian, Florian Rist, Helmut Pottmann, and Christian Müller. 2020. Principal symmetric meshes. *ACM Trans. Graph.* 39, 4 (2020), 127:1–17.
Jesús Pérez, Miguel A Otaduy, and Bernhard Thomaszewski. 2017. Computational design and automated fabrication of Kirchhoff-plateau surfaces. *ACM Trans. Graph.* 36, 4 (2017), 62:1–12.
Stefan Pillwein, Kurt Leimer, Michael Birsak, and Przemyslaw Musialski. 2020. On Elastic Geodesic Grids and Their Planar to Spatial Deployment. *ACM Trans. Graph.* 39, 4 (2020), 125:1–12.
Helmut Pottmann, Qixing Huang, Bailin Deng, Alexander Schiftner, Martin Kilian, Leonidas Guibas, and Johannes Wallner. 2010. Geodesic patterns. *ACM Trans. Graph.* 29, 4 (2010), 43:1–10.
Hartmut Prautzsch, Wolfgang Boehm, and Marco Paluszny. 2002. *Bézier and B-Spline Techniques*. Springer-Verlag.
Yingying Ren, Uday Kusupati, Julian Panetta, Florin Isvoranu, Davide Pellis, Tian Chen, and Mark Pauly. 2022. Umbrella Meshes: Elastic Mechanisms for Freeform Shape Deployment. *ACM Trans. Graph.* 41, 4 (2022), 152:1–15.
Yingying Ren, Julian Panetta, Tian Chen, Florin Isvoranu, Samuel Poincloux, Christopher Brandt, Alison Martin, and Mark Pauly. 2021. 3D weaving with curved ribbons. *ACM Trans. Graph.* 40, 4 (2021), 127:1–15.
Andrew O. Sageman-Furnas, Albert Chern, Mirela Ben-Chen, and Amir Vaxman. 2019. Chebyshev Nets from Commuting PolyVector Fields. *ACM Trans. Graph.* 38, 6 (2019), 172:1–16.
Eike Schling, Martin Kilian, Hui Wang, Jonas Schikore, and Helmut Pottmann. 2018. Design and construction of curved support structures with repetitive parameters. In *Advances in architectural geometry 2018*, Lars Hesselgren et al. (Eds.). 140–165.
Eike Schling and Jonas Schikore. 2023. Morphology of Kinetic Asymptotic Grids. In *Towards Radical Regeneration*, Christoph Gengnagel et al. (Eds.). Springer International Publishing, 374–393.
Eike Schling, Hui Wang, Sebastian Hoyer, and Helmut Pottmann. 2022. Designing asymptotic geodesic hybrid gridshells. *Computer-Aided Design* 152 (2022), 103378:1–17.
Enrique Soriano, Ramon Sastre, and Dionis Boixader. 2019. G-shells: Flat collapsible geodesic mechanisms for gridshells. In *Proc. of IASS annual symposia 2019*. Int. Ass. for Shell and Spatial Structures (IASS), 1–8.
Chengcheng Tang, Xiang Sun, Alexandra Gomes, Johannes Wallner, and Helmut Pottmann. 2014. Form-finding with Polyhedral Meshes Made Simple. *ACM Trans. Graph.* 33, 4 (2014), 70:1–9.
Xavier Tellier. 2022a. Bundling elastic gridshells with alignable nets. Part I: Analytical approach. *Automation in Construction* 141 (2022), 104291.
Xavier Tellier. 2022b. Bundling elastic gridshells with alignable nets. Part II: Form-finding. *Automation in Construction* 141 (2022), 104292.
Tom Van Mele, Niels De Temmerman, Lars De Laet, and Marijke Mollaert. 2010. Scissor-hinged retractable membrane structures. *Int. J. of Structural Engineering* 1, 3-4 (2010), 374–396.
Bolun Wang, Hui Wang, Eike Schling, and Helmut Pottmann. 2023. Rectifying Strip Patterns. *ACM Trans. Graph.* 42, 6 (2023), 256:1–18.
Hui Wang, Davide Pellis, Florian Rist, Helmut Pottmann, and Christian Müller. 2019. Discrete geodesic parallel coordinates. *ACM Trans. Graph.* 38, 6 (2019), 173:1–13.

APPENDIX

A FORMS ON SURFACES

This section provides a brief introduction to forms on surfaces. Comprehensive treatments of this topic can be found in [O'Neill 2006] and [Needham 2021].

A.1 Tangent vectors and 1-forms

Let $\mathcal{S}$ be a smooth surface in three-dimensional Euclidean space. At a point P of the surface, the tangent plane $T_{\mathcal{S}_P}$ is defined as the space of all vectors $\mathbf{v}$ tangent to the surface $\mathcal{S}$ at P. Suppose we have selected two tangent vectors $\mathbf{b}_1$ and $\mathbf{b}_2 \in T_{\mathcal{S}_P}$. If these vectors do not lie along the same line, every tangent vector $\mathbf{v} \in T_{\mathcal{S}_P}$ can be written as a linear combination of them as

$$\mathbf{v} = v^1\mathbf{b}_1 + v^2\mathbf{b}_2,$$

where the scalars v^1 and v^2 are the components of $\mathbf{v}$. The set $\{\mathbf{b}_1, \mathbf{b}_2\}$ then forms a basis for the tangent vector space $T_{\mathcal{S}_P}$.

Now, consider a real-valued function that takes a single tangent vector $\mathbf{v} \in T_{\mathcal{S}_P}$ as input and is linear in its input $\mathbf{v}$. Such an object is called a *1-form*. More explicitly, if $\mathbf{v}$ and $\mathbf{w}$ are two tangent vectors of $T_{\mathcal{S}_P}$, and f, g are two scalars, a 1-form is defined by the following property:

$$\boldsymbol{\omega}(f\mathbf{v} + g\mathbf{w}) = f\boldsymbol{\omega}(\mathbf{v}) + g\boldsymbol{\omega}(\mathbf{w}).$$

Given two 1-forms $\boldsymbol{\omega}$ and $\boldsymbol{\nu}$, we can define their sum and multiplication with scalars as

$$(\boldsymbol{\omega} + \boldsymbol{\nu})(\mathbf{v}) = \boldsymbol{\omega}(\mathbf{v}) + \boldsymbol{\nu}(\mathbf{v}) \quad \text{and} \quad (f\boldsymbol{\omega})(\mathbf{v}) = f\boldsymbol{\omega}(\mathbf{v}),$$

under which the space of 1-forms constitutes a vector space. This vector space is said to be a *dual space* of the tangent vector space $T_{\mathcal{S}_P}$ in which it acts, and it is denoted as $T^*_{\mathcal{S}_P}$. To understand this duality, consider a vector $\mathbf{v}$ as a function that acts on 1-forms $\boldsymbol{\omega}$, defined by $\mathbf{v}(\boldsymbol{\omega}) \equiv \boldsymbol{\omega}(\mathbf{v})$. With this definition, the actions of vectors on 1-forms and vice versa are symmetric, indicating that these spaces are dual to each other.

If we select a basis $\{\mathbf{b}_1, \mathbf{b}_2\}$ of $T_{\mathcal{S}_P}$, we can define a *dual-basis* $\{\boldsymbol{\eta}^1, \boldsymbol{\eta}^2\}$ for the vector space $T^*_{\mathcal{S}_P}$ such that

$$\boldsymbol{\eta}^i(\mathbf{b}_j) = \delta^i_j, \tag{A.1}$$

with $i, j \in \{1, 2\}$, and where δ^i_j is the Kronecker delta. A 1-form $\boldsymbol{\omega}$ of $T^*_{\mathcal{S}_P}$ can now be written as

$$\boldsymbol{\omega} = \omega_1\boldsymbol{\eta}^1 + \omega_2\boldsymbol{\eta}^2,$$

where the scalars ω_1 and ω_2 are the components of $\boldsymbol{\omega}$. Note that

$$\boldsymbol{\omega}(\mathbf{b}_1) = \omega_1, \quad \text{and} \quad \boldsymbol{\omega}(\mathbf{b}_2) = \omega_2.$$

In components, the function $\boldsymbol{\omega}(\mathbf{v})$ is therefore evaluated as $\boldsymbol{\omega}(\mathbf{v}) = v^1\omega_1 + v^2\omega_2$. Note that $\boldsymbol{\eta}^i(\mathbf{v}) = v^i$, meaning the basis 1-form $\boldsymbol{\eta}^i$ extracts the i-th component of the vector $\mathbf{v}$.

A.2 Wedge product and 2-forms

We define a second object that acts on tangent vectors of the surface $\mathcal{S}$, called a *2-form*. A 2-form $\boldsymbol{\omega}$ is a real-valued function on all ordered pairs of tangent vectors $\mathbf{v}, \mathbf{w} \in T_{\mathcal{S}_P}$ such that $\boldsymbol{\omega}(\mathbf{v}, \mathbf{w})$ is linear in $\mathbf{v}$, $\mathbf{w}$, and anti-symmetric, i.e., $\boldsymbol{\omega}(\mathbf{v}, \mathbf{w}) = -\boldsymbol{\omega}(\mathbf{w}, \mathbf{v})$. The property of anti-symmetry entails that $\boldsymbol{\omega}(\mathbf{v}, \mathbf{v}) = 0$.

It is possible to generate a 2-form from the combination of two 1-forms by defining a new operation between forms, known as the *wedge product*, denoted by the symbol $\wedge$. When given two 1-forms $\boldsymbol{\omega}$ and $\boldsymbol{\nu}$, their *wedge product* $\boldsymbol{\omega} \wedge \boldsymbol{\nu}$ is defined as the 2-form such that

$$(\boldsymbol{\omega} \wedge \boldsymbol{\nu})(\mathbf{v}, \mathbf{w}) = \boldsymbol{\omega}(\mathbf{v})\boldsymbol{\nu}(\mathbf{w}) - \boldsymbol{\omega}(\mathbf{w})\boldsymbol{\nu}(\mathbf{v}).$$

The wedge product $\boldsymbol{\omega} \wedge \boldsymbol{\nu}$ is linear and anti-symmetric with respect to the input vectors $\mathbf{v}$, $\mathbf{w}$, and therefore it is a 2-form. Note that this

definition also leads to a second anti-symmetry property: $\boldsymbol{\omega} \wedge \boldsymbol{\nu} = -\boldsymbol{\nu} \wedge \boldsymbol{\omega}$, which, in turn, implies $\boldsymbol{\omega} \wedge \boldsymbol{\omega} = 0$.

It is evident that the addition of two 2-forms results in another 2-form, and similarly, when multiplied by a constant, a 2-form remains a 2-form. Consequently, 2-forms constitute a vector space, making it natural to search for a basis for this space. Writing the 1-forms $\boldsymbol{\omega}$ and $\boldsymbol{\nu}$ in a basis $\{\boldsymbol{\eta}^1, \boldsymbol{\eta}^2\}$ and applying the anti-symmetry of the wedge product, we get

$$\begin{aligned}\boldsymbol{\omega} \wedge \boldsymbol{\nu} &= (\omega_1 \boldsymbol{\eta}^1 + \omega_2 \boldsymbol{\eta}^2) \wedge (\nu_1 \boldsymbol{\eta}^1 + \nu_2 \boldsymbol{\eta}^2) \\ &= \omega_1 \nu_1 \, \boldsymbol{\eta}^1 \wedge \boldsymbol{\eta}^1 + \omega_1 \nu_2 \, \boldsymbol{\eta}^1 \wedge \boldsymbol{\eta}^2 + \omega_2 \nu_1 \, \boldsymbol{\eta}^2 \wedge \boldsymbol{\eta}^1 + \omega_2 \nu_2 \, \boldsymbol{\eta}^2 \wedge \boldsymbol{\eta}^2 \\ &= (\omega_1 \nu_2 - \omega_2 \nu_1) \, \boldsymbol{\eta}^1 \wedge \boldsymbol{\eta}^2.\end{aligned}$$

We can see that the 2-form $\boldsymbol{\eta}^1 \wedge \boldsymbol{\eta}^2$ constitutes a basis for the 2-forms acting on the tangent vectors of $T_{\mathcal{S}_P}$. Note that the basis comprises a single element.

More generally, the degree p of a p-form is defined as the number of its vector inputs. In this view, a scalar function on the surface $\mathcal{S}$ can be interpreted as a *0-form*. It is also possible to define forms of higher degree involving more input vectors by extending the wedge product to three or more 1-forms. However, in a two-dimensional space like $T_{\mathcal{S}_P}$, the wedge product of three or more 1-form basis elements will always contain a repeated element, and as a consequence, it is always zero. Therefore, in $T_{\mathcal{S}_P}$ the forms of higher degree are 2-forms.

A.3 Exterior derivative

To quantify how much a form varies on the surface $\mathcal{S}$ as we move away from a point $P_0 \in \mathcal{S}$, we introduce a powerful tool called the *exterior derivative*. Starting with a 0-form $f(P)$, where the dependence of f on a surface point P is explicitly stated, we calculate its directional derivative along a tangent vector $\mathbf{v}$ at a point P_0. To do so, consider a surface curve $C = P(r)$, parametrized by a parameter r, with $P(0) = P_0$ and $P'(0) = \mathbf{v}$, where prime denotes differentiation with respect to r. The exterior derivative of f, denoted as $\mathbf{d}f$, is defined as the 1-form such that

$$\mathbf{d}f(\mathbf{v}) = f'(P(r))\big|_{r=0}.$$

We can extend the exterior derivative to forms of higher degrees as the unique function that maps p-forms to $(p+1)$-forms with the properties

$$\mathbf{d}(\boldsymbol{\omega} \wedge \boldsymbol{\nu}) = \mathbf{d}\boldsymbol{\omega} \wedge \boldsymbol{\nu} + (-1)^k \boldsymbol{\omega} \wedge \mathbf{d}\boldsymbol{\nu}, \quad \text{and} \quad \mathbf{d}\mathbf{d}\boldsymbol{\omega} = 0, \tag{A.2}$$

where $\boldsymbol{\omega}$ and $\boldsymbol{\nu}$ are forms of any degree, and k is the degree of the form $\boldsymbol{\omega}$. Considering the wedge product of a scalar with a form as a multiplication, Equations A.2 also entails

$$\mathbf{d}(f\boldsymbol{\omega}) = \mathbf{d}f \wedge \boldsymbol{\omega} + f\mathbf{d}\boldsymbol{\omega}.$$

To compute the exterior derivative of a 1-form $\boldsymbol{\omega}$, we can first represent it in a dual-basis $\{\mathbf{d}u, \mathbf{d}v\}$ as $\boldsymbol{\omega} = \omega_1 \mathbf{d}u + \omega_2 \mathbf{d}v$, where u and v are two scalar functions fulfilling $\mathbf{d}u \wedge \mathbf{d}v \neq 0$ (a parametrization). Then, Equations A.2 yields

$$\mathbf{d}\boldsymbol{\omega} = \mathbf{d}\omega_1 \wedge \mathbf{d}u + \mathbf{d}\omega_2 \wedge \mathbf{d}v,$$

where $\mathbf{d}\boldsymbol{\omega}$ is a 2-form. Since 3-forms vanish on a surface $\mathcal{S}$, the exterior derivative of a 2-form also vanishes.

A.4 Integration of forms

A p-form is specifically designed for integration over a p-dimensional domain. For instance, a 0-form is intended for integration (evaluation) at a point, which is 0-dimensional. Moving up a dimension, a 1-form is tailored for integration along oriented lines. In particular, the integral of a 1-form along a curve $C = P(t)$, parametrized by $t \in [t_0, t_1]$, with a velocity tangent vector $\mathbf{v}(t) = P'(r)$, is defined as

$$\int_C \boldsymbol{\omega} = \int_{r_0}^{r_1} \boldsymbol{\omega}(\mathbf{v}(r))\mathrm{d}r. \tag{A.3}$$

Similarly, 2-forms are apt for integration over oriented areas.

Consider now a p-dimensional oriented region $\mathcal{R}$ and its boundary $\partial\mathcal{R}$. To illustrate, if $\mathcal{R}$ is an oriented line, $\partial\mathcal{R}$ signifies the endpoints with consistent orientation. Alternatively, if $\mathcal{R}$ represents a 2D region with an established orientation, $\partial\mathcal{R}$ becomes the boundary curve consistently oriented. Let $\boldsymbol{\omega}$ be a p-form and $\mathcal{R}$ a $(p+1)$-dimensional region, Stokes' theorem states that

$$\int_{\partial\mathcal{R}} \boldsymbol{\omega} = \int_{\mathcal{R}} \mathbf{d}\boldsymbol{\omega}. \tag{A.4}$$

B APPENDIX OF THEOREMS

Proposition 8. *Let $\{C^1, C^3\}$ be a curve net on a smooth surface $\mathcal{S}$. Let $\boldsymbol{\omega}$ be a smooth 2-form on $\mathcal{S}$, and let $\mathcal{R}$ be a region enclosed by a net-loop $\partial\mathcal{R}$. If*

$$\int_{\mathcal{R}} \boldsymbol{\omega} = 0, \quad \textit{for all net-loops } \partial\mathcal{R},$$

then $\boldsymbol{\omega} = 0$ at every point of $\mathcal{S}$.

Proof. Consider a net-loop $\partial\mathcal{R}$ which bounds a region $\mathcal{R}$ homeomorphic to a disk, orient consistently the curve net inside $\mathcal{R}$, and consider the dual-basis $\{\boldsymbol{\eta}^1, \boldsymbol{\eta}^3\}$. At every point on $\mathcal{R}$, the 2-form $\boldsymbol{\omega}$ can be expressed as $\boldsymbol{\omega} = f\,\boldsymbol{\eta}^1 \wedge \boldsymbol{\eta}^3$, where f is a smooth scalar function. For a non-degenerate curve net, the 2-form $\boldsymbol{\eta}^1 \wedge \boldsymbol{\eta}^3$ is consistently oriented and non-vanishing, meaning its integral is strictly positive (or strictly negative) for every non-empty region $\mathcal{R}' \subseteq \mathcal{R}$. Suppose, for the sake of contradiction, that f is positive (or negative) at some point within $\mathcal{R}$. Since f is smooth, there exists a smaller region $\mathcal{R}' \subset \mathcal{R}$ around this point, bounded by a net-loop $\partial\mathcal{R}'$, where f is strictly positive (or strictly negative). This would imply

$$\int_{\mathcal{R}'} f\,\boldsymbol{\eta}^1 \wedge \boldsymbol{\eta}^3 = \int_{\mathcal{R}'} \boldsymbol{\omega} > 0 \quad (\text{or} < 0),$$

which contradicts the statement. Therefore, since a smooth surface $\mathcal{S}$ can be covered by regions homeomorphic to a disk, f must be identically zero everywhere on $\mathcal{S}$, which implies $\boldsymbol{\omega} = 0$ at every point of $\mathcal{S}$. □

Proposition 9. *If in an orthogonal curve net $\{C^1, C^2\}$ curves C^1 are geodesics and curves C^2 have constant geodesic curvature along their path, then the net lies on a surface isometric to a surface of revolution.*

Proof. Consider a surface parametrization $S(u, v)$, where the u-curves and v-curves are given respectively by C^1 and C^2. Let E, F, and G be the coefficients of the first fundamental form of the parametrization $S(u, v)$, as defined by Equations 4.3. Since this

parametrization is orthogonal, we have $\boldsymbol{\theta}^1 = \sqrt{E}\,\mathbf{d}u$ and $\boldsymbol{\theta}^2 = \sqrt{G}\,\mathbf{d}v$. Considering that $\boldsymbol{\theta}^1 \wedge \boldsymbol{\theta}^2 = \sqrt{EG}\,\mathbf{d}u \wedge \mathbf{d}v$, from first Cartan structural equations 2.13, we get:

$$g_1 = -\frac{E_{,v}}{2E\sqrt{G}}, \quad g_2 = \frac{G_{,u}}{2G\sqrt{E}}. \tag{B.1}$$

Since $g_1 = 0$, we deduce $E_{,v} = 0$. E is then a function of u only. Similarly, since also g_2 is a function of u only, the function $G_{,u}/G$ depends solely on u as well. Let u_a, u_b be two parameters within the u-domain of the surface. For every fixed v-parameter v', we can then write:

$$\int_{u_a}^{u_b} \frac{G_{,u}(u, v')}{G(u, v')}\,\mathrm{d}u = \ln G(u_b, v') - \ln G(u_a, v') = f(u), \tag{B.2}$$

where f is a scalar function of u only. This implies

$$\frac{G(u_b, v')}{G(u_a, v')} = h(u), \quad \text{for any } u_a, u_b, \tag{B.3}$$

where h is another scalar function of u only. As shown in Proposition 4.2 of [Wang et al. 2019], Equation B.3, together with $g_1 = 0$, implies that the surface $S(u, v)$ is isometric to a surface of revolution. □

Derivations of Theorem 2, Equations 3.14.

$$\begin{aligned}
\mathbf{d}t_1(\mathbf{e}_1) - \mathbf{d}n_1(\mathbf{e}_2) &= g_1(n_2 - n_1) - 2g_2 t_1 \\
&= g_1(n_2 - n_1) - 2(\kappa_I - \kappa_{II})(g_3 \csc 2\beta - g_1 \cot 2\beta \\
&\quad - \mathbf{d}\alpha(\mathbf{e}_3) \csc 2\beta) \sin\beta \cos\beta \\
&= (\kappa_{II} - \kappa_I) g_1 (\cos^2\beta - \sin^2\beta) + (\kappa_{II} - \kappa_I)(g_3 \\
&\quad - g_1(\cos^2\beta - \sin^2\beta) - \mathbf{d}\alpha(\mathbf{e}_3)) \\
&= (\kappa_{II} - \kappa_I)(g_3 - \mathbf{d}\alpha(\mathbf{e}_3)).
\end{aligned}$$

$$\begin{aligned}
\mathbf{d}t_3(\mathbf{e}_3) - \mathbf{d}n_3(\mathbf{e}_4) &= g_3(n_2 - n_1) + 2g_4 t_1 \\
&= g_3(n_2 - n_1) + 2(\kappa_{II} - \kappa_I)(g_1 \csc 2\beta - g_3 \cot 2\beta \\
&\quad + \mathbf{d}\alpha(\mathbf{e}_1) \csc 2\beta) \sin\beta \cos\beta \\
&= (\kappa_{II} - \kappa_I) g_3 (\cos^2\beta - \sin^2\beta) + (\kappa_{II} - \kappa_I)(g_1 \\
&\quad - g_3(\cos^2\beta - \sin^2\beta) + \mathbf{d}\alpha(\mathbf{e}_1)) \\
&= (\kappa_{II} - \kappa_I)(g_1 + \mathbf{d}\alpha(\mathbf{e}_1)).
\end{aligned}$$

C NORMAL CURVATURE-PRESERVING CHEBYSHEV NETS

The conditions for a surface to admit the existence of a normal curvature-preserving Chebyshev net have been established by Liu et al. [2023] (see Table 1). Their proof relies on a mesh discretization of the net — a quad mesh with equal edge lengths that collapses into a planar polyline while preserving edge lengths and discrete normal curvatures, referred to as a *generalized C-mesh*. The following theorem establishes the continuous counterpart of these conditions:

Theorem 3. *A normal curvature-preserving Chebyshev net exists only on surfaces of revolution and cylindrical surfaces.*

Proof. From Equations 3.14 of Theorem 2, imposing the Chebyshev conditions of Proposition 7, we get the additional constraint:

$$\mathbf{d}n_1(\mathbf{e}_2) = \mathbf{d}t_1(\mathbf{e}_1). \tag{C.1}$$

Consider a double frame associated with the Chebyshev net $\{C^1, C^3\}$, together with the principal curvature net $\{C^5, C^6\}$. Theorem 2 entails that the principal curvature net bisects the Chebyshev net, and that $n_1 = n_3$ and $t_1 = t_3$ are constant along curves C^6. Let $\{\boldsymbol{\theta}^5, \boldsymbol{\theta}^6\}$ be the dual-basis of $\{\mathbf{e}_5, \mathbf{e}_6\}$. Proposition 2 entails then $\mathbf{d}n_1 \wedge \boldsymbol{\theta}^5 = 0$ and $\mathbf{d}t_1 \wedge \boldsymbol{\theta}^5 = 0$. Thus we can write:

$$\mathbf{d}n_1 = f\,\boldsymbol{\theta}^5, \quad \mathbf{d}t_1 = h\,\boldsymbol{\theta}^5, \tag{C.2}$$

with f and h being two scalar functions. Let β be the angle that $\mathbf{e}_1$ makes with the principal curvature direction $\mathbf{e}_5$. We can then write

$$\mathbf{e}_1 = \cos\beta\,\mathbf{e}_5 - \sin\beta\,\mathbf{e}_6, \quad \mathbf{e}_2 = \sin\beta\,\mathbf{e}_5 + \cos\beta\,\mathbf{e}_6.$$

Plugging these vectors into Equation C.1, with Equations C.2 we get $f \sin\beta = h\cos\beta$, and then

$$\mathbf{d}n_1 = f\,\boldsymbol{\theta}^5, \quad \mathbf{d}t_1 = f\tan\beta\,\boldsymbol{\theta}^5.$$

Enforcing the vanishing of the exterior derivative of $\mathbf{d}n_1$, we get:

$$\mathbf{d}\mathbf{d}n_1 = f\,\mathbf{d}\boldsymbol{\theta}_5 - \mathbf{d}f(\mathbf{e}_6)\,\boldsymbol{\theta}^5 \wedge \boldsymbol{\theta}^6 = 0.$$

Considering that, for Equations 2.13, $\mathbf{d}\boldsymbol{\theta}^5 = g_5\,\boldsymbol{\theta}^5 \wedge \boldsymbol{\theta}^6$, this yields

$$\mathbf{d}f(\mathbf{e}_6) = f g_5. \tag{C.3}$$

Enforcing now the vanishing of the exterior derivative of $\mathbf{d}t_1$, and using again Equations 2.13, we get:

$$\mathbf{d}\mathbf{d}t_1 = \left(f g_5 \tan\beta - \tan\beta\,\mathbf{d}f(\mathbf{e}_6) - f\sec^2\beta\,\mathbf{d}\beta(\mathbf{e}_6)\right)\,\boldsymbol{\theta}^5 \wedge \boldsymbol{\theta}^6 = 0.$$

Substituting Equation C.3, this yields:

$$f\sec^2\beta\,\mathbf{d}\beta(\mathbf{e}_6) = 0. \tag{C.4}$$

If $f \neq 0$, and therefore $\mathbf{d}n_1 \neq 0$, this implies $\mathbf{d}\beta(\mathbf{e}_6) = 0$. For Proposition 4, this entails $\mathbf{d}\beta(\mathbf{e}_1) = \mathbf{d}\beta(\mathbf{e}_3)$. The Chebyshev condition of Equation 3.7 implies then $g_1 = -g_3$. Therefore, summing Equations 3.9, we get $g_5 = 0$. Moreover, from Equation 3.10 and Proposition 3, we deduce $\mathbf{d}g_6(\mathbf{e}_6) = 0$. From Euler equations 2.9, we observe that the conditions $\mathbf{d}n_1(\mathbf{e}_6) = \mathbf{d}t_1(\mathbf{e}_6) = \mathbf{d}\beta(\mathbf{e}_6) = 0$ imply that the principal curvatures κ_I, κ_{II} are constant along curves C^6. Therefore, for Definition 3, $\mathbf{d}n_5(\mathbf{e}_6) = \mathbf{d}n_6(\mathbf{e}_6) = 0$. Moreover, for principal curvature lines, we have $t_5 = t_6 = 0$. From Equations 2.6, 2.7, and 2.8, the conditions $g_5 = t_5 = 0$ imply $\tau_5 = 0$, $n_5 = \kappa_5$, and therefore $\mathbf{d}\kappa_5(\mathbf{e}_6) = 0$. Similarly, $\mathbf{d}g_6(\mathbf{e}_6) = \mathbf{d}n_6(\mathbf{e}_6) = t_6 = 0$ imply $\tau_6 = 0$ and $\mathbf{d}\kappa_6(\mathbf{e}_6) = 0$. In summary, $\tau_5 = \mathbf{d}\kappa_5(\mathbf{e}_6) = 0$ indicates that curves C^5 are congruent and planar, while $\tau_6 = \mathbf{d}\kappa_6(\mathbf{e}_6) = 0$ indicates that curves C^6 are circular arcs. Thus, since this net is orthogonal, the surface is a surface of revolution. When $\kappa_{II} = 0$, we obtain a cylindrical surface. □

Corollary 4. *A constant normal curvature Chebyshev net exists only on linear Weingarten surfaces of hyperbolic type.*

Proof. In this case, we have $\mathbf{d}n_1 = 0$, and therefore Equation C.4 is satisfied for $\mathbf{d}\beta(\mathbf{e}_6) \neq 0$. Equation C.1 entails $\mathbf{d}t_1 = 0$. From equation 3.16, we observe that the linear relation $aK + bH + c = 0$ holds on the entire surface with constant coefficients a, b and c. □

Corollary 5. *An asymptotic Chebyshev net exists only on K-surfaces.*

Proof. We have now $n_1 = 0$, and therefore $b = 0$. From Corollary 4, we get $K = -c/a$, which is a non-positive constant. □